Sister Rod Destructive Examinations (FY21)

Appendix I: SNF Aerosols Released During Rod Fracture

Spent Fuel and Waste Disposition

Prepared for
US Department of Energy

Spent Fuel and Waste Science and Technology

Oak Ridge National Laboratory
Rose Montgomery, Yadu Sasikumar, Tammy Keever, Vineet Kumar

March 31, 2022

M2SF-22OR010201042

ORNL/SPR-2021/2282

This report was prepared as an account of work sponsored by an agency of the United States Government. Neither the United States Government nor any agency thereof, nor any of their employees, makes any warranty, express or implied, or assumes any legal liability or responsibility for the accuracy, completeness, or usefulness of any information, apparatus, product, or process disclosed, or represents that its use would not infringe privately owned rights. Reference herein to any specific commercial product, process, or service by trade name, trademark, manufacturer, or otherwise, does not necessarily constitute or imply its endorsement, recommendation, or favoring by the United States Government or any agency thereof. The views and opinions of authors expressed herein do not necessarily state or reflect those of the United States Government or any agency thereof.

SUMMARY

This report documents work performed under the Spent Fuel and Waste Disposition's Spent Fuel and Waste Science and Technology program for the US Department of Energy (DOE) Office of Nuclear Energy (NE). This work was performed to fulfill Level 2 Milestone M2SF-22OR010201042, "FY2021 ORNL Report on High Burnup Sibling Pin Testing Results," within work package SF-22OR01020104 and is an update to the work reported in M2SF-21OR010201032, M2SF-19ORO010201026 and M2SF-19OR010201028.

As a part of the DOE NE High Burnup Spent Fuel Data Project, Oak Ridge National Laboratory (ORNL) is performing destructive examinations (DEs) of high burnup (HBU) (>45 GWd/MTU) spent nuclear fuel (SNF) rods from the North Anna Nuclear Power Station operated by Dominion Energy. The SNF rods, called *sister rods* or *sibling rods*, are all HBU and include four different kinds of fuel rod cladding: standard Zircaloy-4 (Zirc-4), low-tin Zirc-4, ZIRLO, and M5. The DEs are being conducted to obtain a baseline of the HBU rods' condition before dry storage and are focused on understanding overall SNF rod strength and durability. Fuel rods and defueled cladding will be tested to derive material properties. Although the data generated can be used for multiple purposes, one primary goal for obtaining the post-irradiation examination data and the associated measured mechanical properties is to support SNF dry storage licensing and relicensing activities by (1) addressing identified knowledge gaps and (2) enhancing the technical basis for post-storage transportation, handling, and subsequent disposition.

This report documents the status of the ORNL Phase 1 DE activities related to the collection of SNF aerosol particles released during fuel rod fracture in 4-point bending in Phase 1 of the sister rod test program.

Table IS-1 summarizes the status of the work.

Table IS-1. DE status.

Planned DE		Status	Comments
AERO	Collect aerosol particles released during selected tests	In progress	An aerosol collection system with fixturing and sampling devices was designed to characterize and quantify the respirable fraction of UO_2 particles released during rod fracture. The fixture is used in conjunction with 4-point bend (4PB) tests. The aerosol collection system is currently being revised, tested, and verified out of cell. Modified collection stages were designed and added to allow for a larger range of particle collection using the commercially available Sioutas cascade. Testing and computational fluid dynamics (CFD) simulations indicate adequate system performance. A different commercially available cascade (Marple) may provide better sampling capability for UO_2 and is being considered. The enclosure used may be changed to a different material to avoid any static attraction. One test was completed in cell with a ZIRLO-clad segment, and initial results are available. Further chemical processing is needed to more precisely define the mass of aerosols collected, but the preliminary order of magnitude result is that 4,615.85 µg of dust-type particulate was collected in the test.

This page is intentionally left blank.

ACKNOWLEDGMENTS

Many thanks to our US Department of Energy Office of Nuclear Energy sponsor, Ned Larson, along with the Spent Fuel and Waste Science and Technology storage and transportation program leadership for their continued support. The sister rod project would not have been possible without the vision and support of the Electric Power Research Institute, Westinghouse, Framatome, and Dominion Energy.

This work would not have been possible without the support and expertise provided by the leadership and staff members of ORNL's Irradiated Fuel Examination Laboratory (IFEL) and Radioactive Materials Analytical Laboratory (RMAL). Special thanks go to Jerid Metcalf, John Hinds, and Brian Woody for their assistance with in-cell testing activities. Many thanks to Haley Wightman, Marc Chattin, and Ben Roach for their support in processing and analyzing the specimens at RMAL. We are indebted to Radiological Control Technicians Andrew Greenwood, Scott Gentry, Mark Walls, and Lisa Duncan, and Facilities Manager Steve Vrooman for their support, oversight, and flexibility in the handling and surveillance of the aerosol specimens. Special thanks go to Maintenance Supervisor Mark Neal and his team for their support on all of our projects, and especially for getting the scanning electron microscopy (SEM) room enclosure modified quickly for this experiment. Finally, many thanks are due Mark Delph for his vital support of the deployment of new equipment to the cell, and we appreciate his continued support.

This page is intentionally left blank.

CONTENTS

This page is intentionally left blank.

LIST OF FIGURES

This page is intentionally left blank.

LIST OF TABLES

This page is intentionally left blank.

REVISION HISTORY

Date	Changes
10/29/2021	This is a new appendix reporting the details of SNF aerosol collection during fuel rod fracture in 4-point bending.
3/31/2022	The date and document ID were updated to reflect its M2 status.

This page is intentionally left blank.

ACRONYMS

4PB	4-point bend
AED	aerodynamic equivalent diameter
AERO	aerosol collection capability
ASME	American Society of Mechanical Engineers
BC	boundary condition
CFD	computational fluid dynamics
CIRFT	cyclic integrated reversible-bending fatigue tester
DE	destructive examination
DOE	US Department of Energy
EDX	energy-dispersive x-ray
FHT	full-length fuel rod heat treatment
HBU	high burnup
HPC	high-performance computing
ICP-MS	Inductively coupled plasma mass spectrometry
IFEL	Irradiated Fuel Examination Laboratory
ISO	International Organization of Standardization
LPM	liters per minute
LT	low tin
NCBI	National Center for Biotechnology Information
NE	Office of Nuclear Energy
NEFCD	Nuclear Energy and Fuel Cycle Division
NQA-1	Nuclear Quality Assurance - 1
ORNL	Oak Ridge National Laboratory
PTFE	polytetrafluoroethylene
RANS	Reynolds-Averaged Navier-Stokes
RMAL	Radioactive Materials Analytical Laboratory
RT	room temperature
SEM	scanning electron microscopy
SNF	spent nuclear fuel
SST	sheer stress transport

This page is intentionally left blank.

I-1 Introduction

As a part of the DOE NE High Burnup Spent Fuel Data Project [I-1], Oak Ridge National Laboratory (ORNL) is performing destructive examinations (DEs) of high burnup (HBU) (>45 GWd/MTU) spent nuclear fuel (SNF) rods from the North Anna Nuclear Power Station operated by Dominion Energy. The SNF rods, called *sister rods* or *sibling rods*, are all HBU and include four different kinds of fuel rod cladding: standard Zircaloy-4 (Zirc-4), low-tin (LT) Zirc-4, ZIRLO, and M5. The Phase 1 DEs [I-2, I-3] are being conducted to obtain a baseline of the HBU rod's condition before dry storage and are focused on understanding overall SNF rod strength and durability. Fuel rods and defueled cladding will be tested to derive material properties. Although the data generated can be used for multiple purposes, one primary goal for obtaining the postirradiation examination data and the associated measured mechanical properties is to support SNF dry storage licensing and relicensing activities by (1) addressing identified knowledge gaps and (2) enhancing the technical basis for post-storage transportation, handling, and subsequent disposition.

To investigate the release of aerosolized radioactive material from a HBU fuel rod during fracture (10 µm or less is generally considered to be the upper limit of human respirability [I-4]), an aerosol collection capability (AERO) is being developed for deployment on the cyclic integrated reversible-bending fatigue tester (CIRFT) equipment (DE.05) and Instron load frame, which is used for DE.07, DE.08, and DE.10. Two different collection configurations are being developed—one for CIRFT and one for the load frame—but the aerosol collection media and approach are expected to be the same. This appendix details the work completed to develop a suitable aerosol collection method for the radioactive materials being examined and provides the results for the first test that was completed in FY21.

I-2 Background

The initial AERO design was configured for the Instron load frame. The initial collection enclosure was a relatively large aluminum box that provided for a large amount of vertical travel for the load frame and fixturing, with the sampling devices mounted on the interior of the box. Several experiments using surrogate materials were completed in FY20; in FY21, the enclosure was downsized to a more compact box with the sampling media mounted externally. The smaller enclosure is 3D printed polyvinyl chloride that can be rinsed, dissolved, or imaged. Sampling tubing fixed in the bottom of the enclosure allows direct access to the location where the material is expected to be expelled from the specimen during 4-point bend (4PB) testing. Illustrations of the collection enclosure are shown in Figure I-1 and Figure I-2.

The initial AERO design included two versions of the aerosol collection cards. The first version had a 4-filter Sioutas cascade impactor [I-5] with particle collection cut points of 2.5, 1.0, 0.50, and 0.25 µm, and the second had a cyclone with a 4 µm cut point. Performance testing of the cyclone indicated that it was not well-suited for this application and its use was discontinued. The cascade impactor type of collection device worked well. In FY21, work focused on expanding the Sioutas cascade impactor to include higher cut point stages to encompass the range of respirable particles and one test was completed with an SNF segment. In late FY21, an alternative, commercially available design, the Marple Cascade Impactor [I-6], was procured for investigation of the design as a better alternative for this application. The Sioutas impactor includes a collection platform fitted with a filter that can be removed for examination of collected material. Experiments were performed using silver filters, because silver can be accommodated in the chemical processing. However, the collected particles were easily dislodged from the silver substrate. To avoid loss of collected material, scanning electron microscopy (SEM) carbon tabs were used in the first test as the collection substrate. Testing indicated that the use of the carbon tabs does not change the collection cut point or capacity; however, chemical processing of the material deposited on the carbon tabs has proven difficult. Each impactor has its own dedicated vacuum pump to maintain the appropriate sampling flow rate.

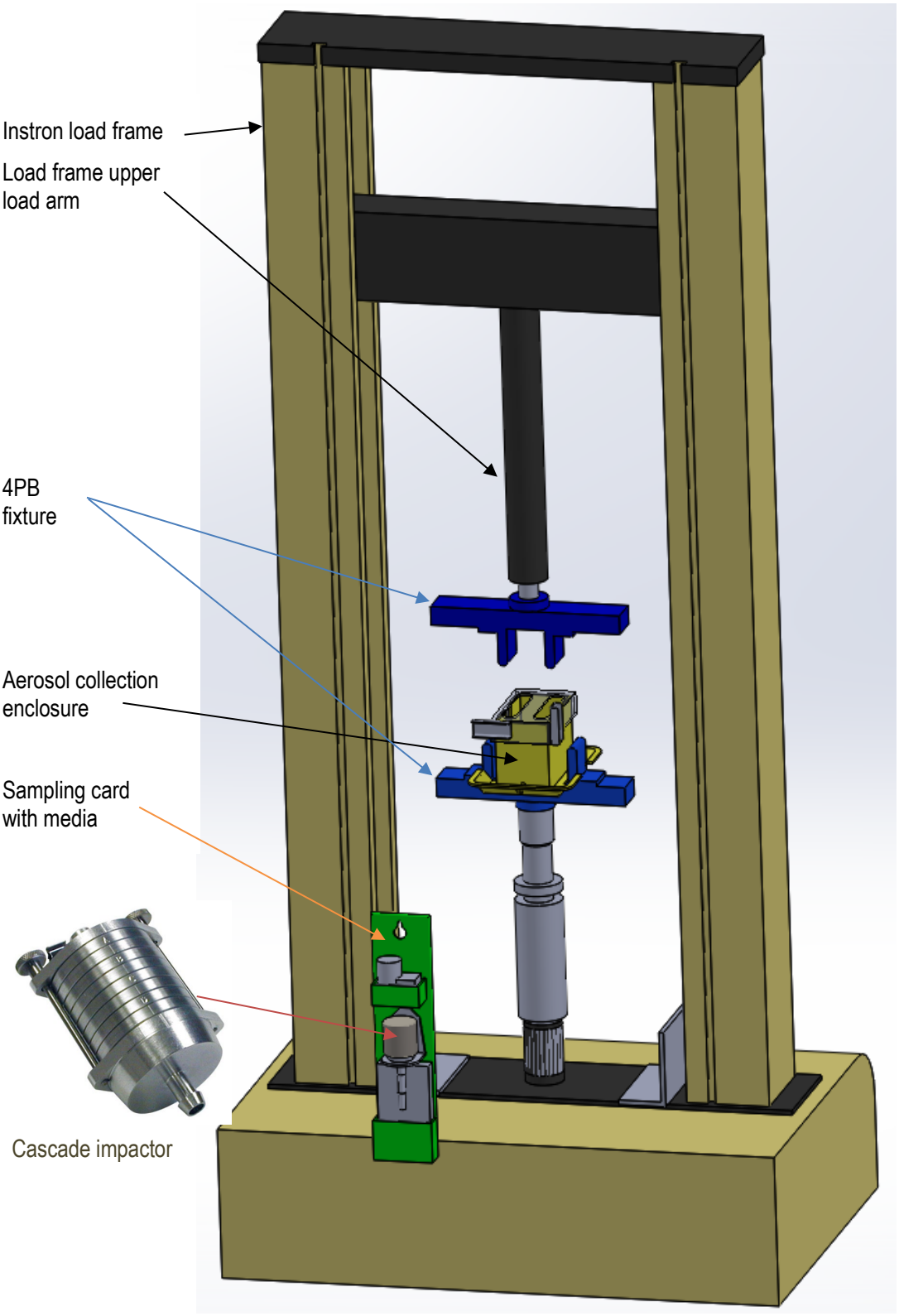

Figure I-1. Illustration of the load frame aerosol collection enclosure with one sampling card shown.

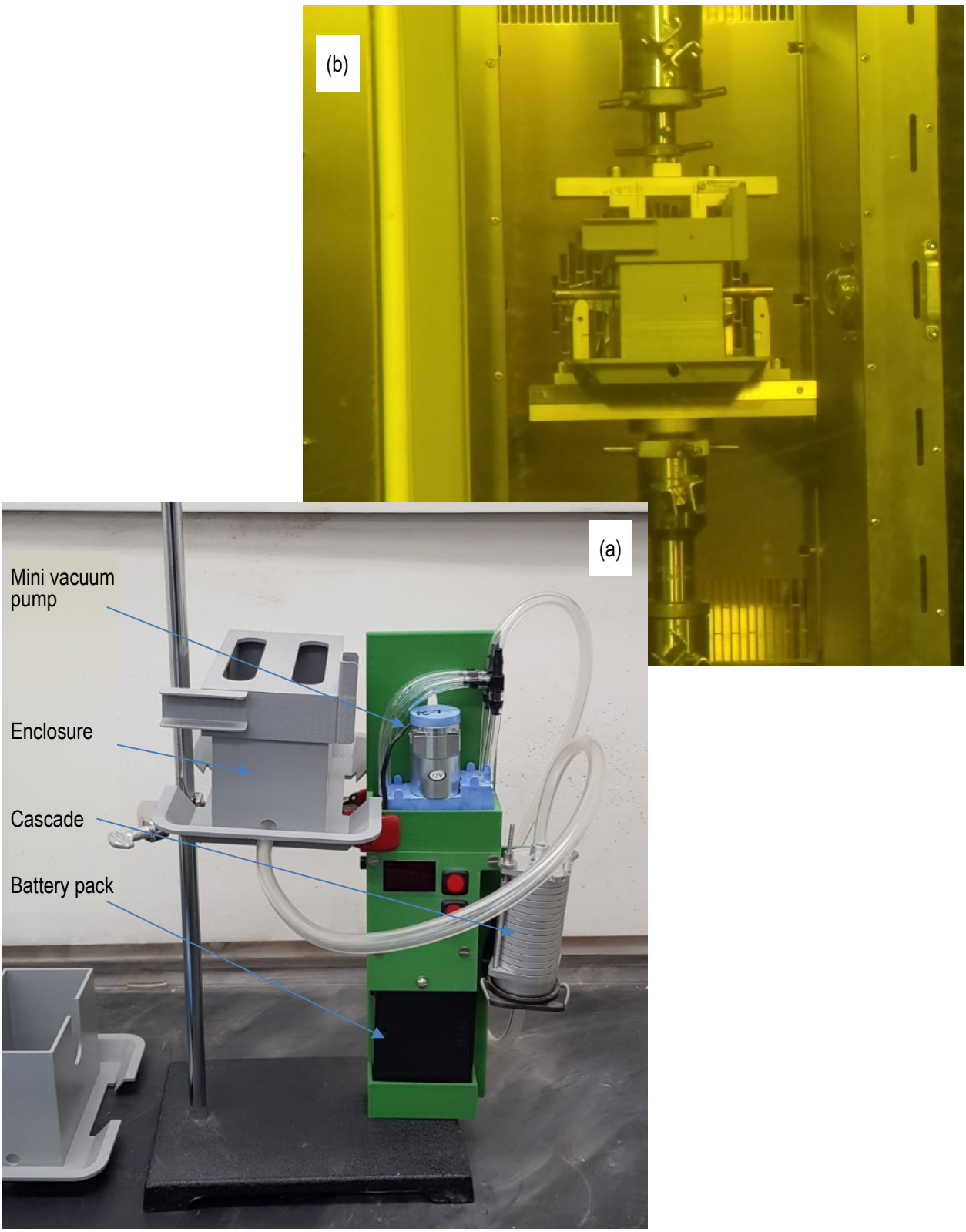

Figure I-2. Sampling card with multistage cascade impactor and dedicated pump (a) set up for verification testing and (b) fit up on the load frame in the hot cell.

I-3 Theory

Inertial impaction is the method selected to collect aerosol particulates released from the sister rod specimen as it is fractured during testing. Impactors are devices that separate the particulates based on size. In an impaction sampler, gas containing the particulates to be sampled is accelerated through an orifice towards a collection filter placed at a fixed distance below an orifice. The collection filter forces the air stream to change direction abruptly, and particles having enough inertia to escape the air stream are collected on the filter. Smaller particles follow the air stream and remain suspended in the gas flow, moving on to the next stage of the impactor (Figure I-3).

The *cut point* of an impaction sampler is the size of particles collected by the sampler with 50% efficiency. Ideally, all particles greater than a certain size are collected on the filter, and all smaller particles pass through. However, because impactors act on aerodynamic variables and do not perform like a mechanical barrier such as a sieve, the collection efficiency is not 100%. Based on the Stokes number (a function of the orifice diameter and flow rate used), the collection efficiency increases for particles larger than the cut point and decreases for smaller particles, as illustrated in Figure I-4. The particle diameter distribution is generally characterized by a log-normal distribution. For a 4 µm cut point, 100% of 10 µm particles and 50% of 4 µm particles are collected from the air stream and deposited on the filter.

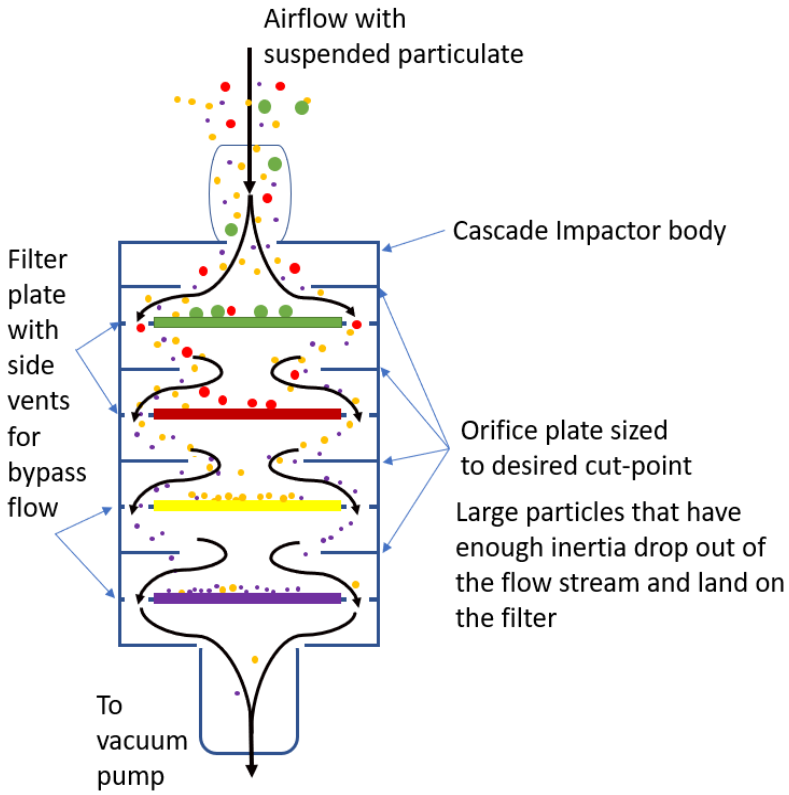

Figure I-3. Schematic showing the principle of inertial impaction as seen in a typical cascade impactor.

Cut points are calculated experimentally using monodisperse powders. The experimental method comprises rigorous sampling techniques involving multiple steps to analyze particulates and compare them with particles at a particular impactor stage, as in the case of cascade impaction cut-point

calculations [I-9]. The efficiency curves are sensitive to the dust-generating conditions, as shown by Moore et al. [I-10], so these must be carried out with great caution to avoid errors.

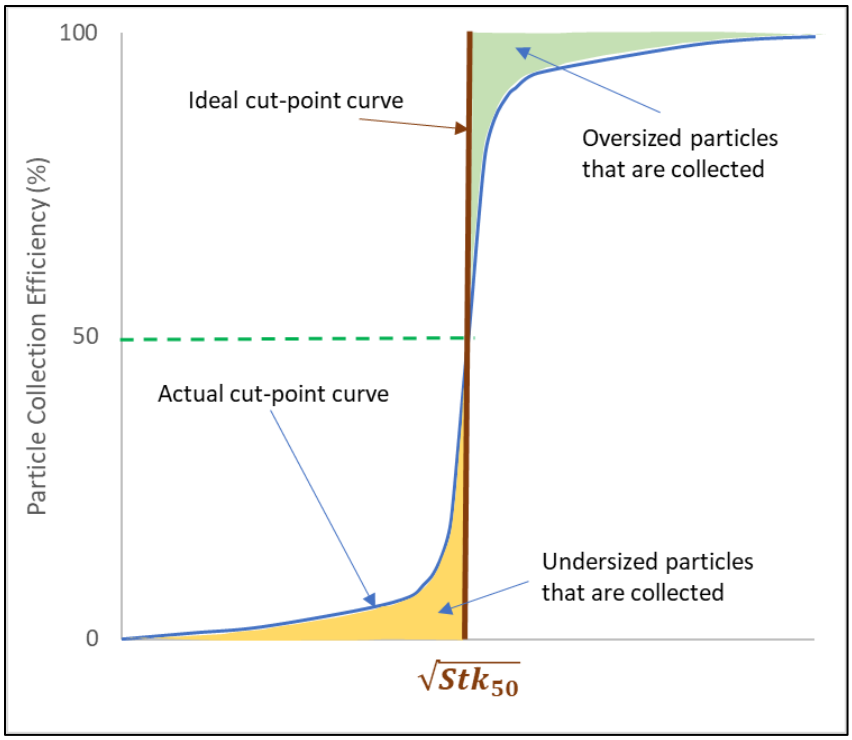

Figure I-4. Illustration of Particle Collection Efficiency in Inertial Impaction Samplers (Adapted from Aerosol Technology, William C. Hinds [G11])

Aerosols consist of two phases: solid/liquid particles and the gas in which they are suspended. The aerosol particles share the temperature, pressure, viscosity, and mean free path of the medium in which they are suspended, and the properties that affect the medium also indirectly affect the aerosol particle motion, an effect which is often Brownian (random) [I-11]. The Reynolds number is an important parameter (ratio of inertial force to frictional force) used to determine whether the flow of an aerosol is laminar or turbulent. In the Stokes region, Re < 1, and in Newton's region Re > 1,000). The region between this, in which 1 < Re < 1,000, is called the *transitional region*. Stokes' law is used for particles in the Stokes region. The law considers particle motion in a fluid in which the inertial forces are negligible compared with viscous forces. This is largely applied to aerosols, as most aerosol motion occurs at low Reynolds numbers (laminar regime) because of the low velocities and small particle sizes involved under settling. The law states that the total resisting force on a spherical particle moving with a velocity V through a fluid is equal to the integration of the normal and tangential forces acting over the surface of the particle:

$$F_D = F_n + F_\tau = \pi\eta V d + 2\pi\eta V d = 3\pi\eta V d, \quad \text{(I-1)}$$

where:

F_D is the total resisting force acting on the particle,
F_n is the normal force acting on the particle,
F_t is the tangential force acting on the particle,

η is the viscosity of the fluid, and
d is the diameter of the particle.

A particle suspended in a medium (for example, air) which eventually settles down has a terminal settling velocity at which the drag force of the air around the aerosol particle is exactly equal and opposite to the force acting on the system (e.g., gravity or centrifugal force). Settling velocity is independent of density of gas and increases rapidly with particle size. In the real world, aerosol particles are composed of different geometries, most often irregular. Therefore, certain correction factors are applied when considering irregular aerosol particle motion, because the shape of the particle affects the drag force and settling velocity. A constant dynamic shape factor (χ) is used to account for the shape effects by multiplying the ratio of the actual resistance force of the non-spherical particle to an equivalent resistance force as experienced on a spherical particle of the same velocity and volume:

$$\chi = \frac{F_D}{3\pi\eta V d_e}. \tag{I-2}$$

The settling velocity of such a spherical particle in terms of d_e for a particle in still air undergoing gravitational settling is given as

$$V_{TS} = \frac{\rho_p {d_e}^2 g}{18\eta\chi}. \tag{I-3}$$

where d_e is the equivalent volume diameter of the sphere for the same volume as that of the irregular particle.

Aerodynamic diameter (d_a) is an equivalent diameter of a water droplet (spherical particle with 1g/cm^3 density) that has the same settling velocity of a non-spherical particle:

$$V_{TS} = \frac{\rho_w {d_a}^2 g}{18\eta}. \tag{I-4}$$

The relationship between the aerodynamic diameter and the equivalent diameter is obtained by comparing the settling velocities obtained for the same particle:

$$d_a = d_e \left(\frac{\rho_p}{\rho_o \chi}\right)^{1/2}. \tag{I-5}$$

For a perfect sphere, the dynamic shape factor (χ) = 1, and the aerodynamic equivalent diameter (AED) is equal to the geometric diameter multiplied by the square root of the relative density of the particle. The dynamic shape factor (χ) is often assumed to be equal to 1 for ease of calculations.

I-3.1 Collection Media Cut Points

Under inertial impaction, the cut point can be calculated at different flow rates for a rectangular jet impactor with jet width *W* and length *L*:

$$d_{50}\sqrt{C_c} = \sqrt{\frac{9\eta W^2 L(Stk_{50})}{\rho_p Q}}. \tag{I-6}$$

where d_{50} is the particle's AED at 50% collection efficiency, *Stk*50 is the Stokes number for 50% collection efficiency for impactors, *Q* is the jet flow rate, *W* and *L* are the width and length of the impactor plate, and *Cc* is Cunningham's slip correction factor. Eq. I-6 is derived from the Stokes number

definition of the ratio of the particle's stopping distance at an average nozzle exit velocity (U) to the impactor opening half width [I-12]:

$$Stk = \frac{\tau U}{W/2} = \frac{\rho_p {d_{50}}^2 U C_c}{9\eta W}, \quad \text{(I-7)}$$

Eq. I-6 can also be written in terms of jet velocities

$$d_{50}\sqrt{C_c} = \sqrt{\frac{9\eta W(Stk_{50})}{\rho_p U}}. \quad \text{(I-8)}$$

I-3.2 Sioutas Cascade Impactor

Initial investigations were focused on implementation of a modified Sioutas cascade impactor sold by SKC Inc. (Sioutas Cascade Impactor Catalog number 225-370). The impactor is constructed from anodized aluminum, has four collection stages with cut points specified at a flow rate of 9 liters per minute (LPM) using polydisperse ammonium sulfate aerosols (density ~1.77 gm/cm^3) as 2.5, 1.0, 0.50, and 0.25 µm AED. This information is summarized in Table I-1, and the equivalent cut point diameters for UO_2 at 9 LPM are also listed. The commercially available Sioutas cascade impactor is shown in Figure I-5.

Table I-1. Manufacturer-specified parameters of the Sioutas cascade impactor at 9 LPM.

Stage	Cascade impactor manufacturer cut-point rating (AED) in µm	Equivalent UO_2 geometric diameter* (µm)	Orifice width (cm)	Orifice length (cm)	Jet velocity (cm/s)
A	2.5	0.75	0.090	1.9	877.2
B	1.0	0.30	0.050	2.1	1,428.6
C	0.5	0.15	0.036	1.9	2,631.6
D	0.25	0.08	0.014	2.5	4,286.0

* AED = geometric diameter × (density)$^{1/2}$

To verify performance of the cascade impactor before using it for tests with SNF, several tests were performed using dusts composed of known materials and diameters. The as-received cascade orifices were measured using a Leica S9i microscope, and the average was taken from five readings. Table I-2 lists the measured orifice dimensions of the purchased stages with the recalculated cut points.

Table I-2. Measured dimensions of the Sioutas cascade impactor using an optical microscope and subsequent new cut-point values calculated using Eq. I-6.

Stage	New cut point diameters (µm)	Equivalent UO2 geometric diameter (µm)	As-received orifice width ± 0.0015 (cm)	As-received orifice length ± 0.0015 (cm)	Average Jet velocity at 9 LPM (cm/s)
PA	3.631	1.097	0.102	2.007	731.0
PB	1.815	0.548	0.051	2.007	1465.0
PC	1.419	0.429	0.039	2.024	1866.0
PD	0.948	0.286	0.026	2.029	2789.0

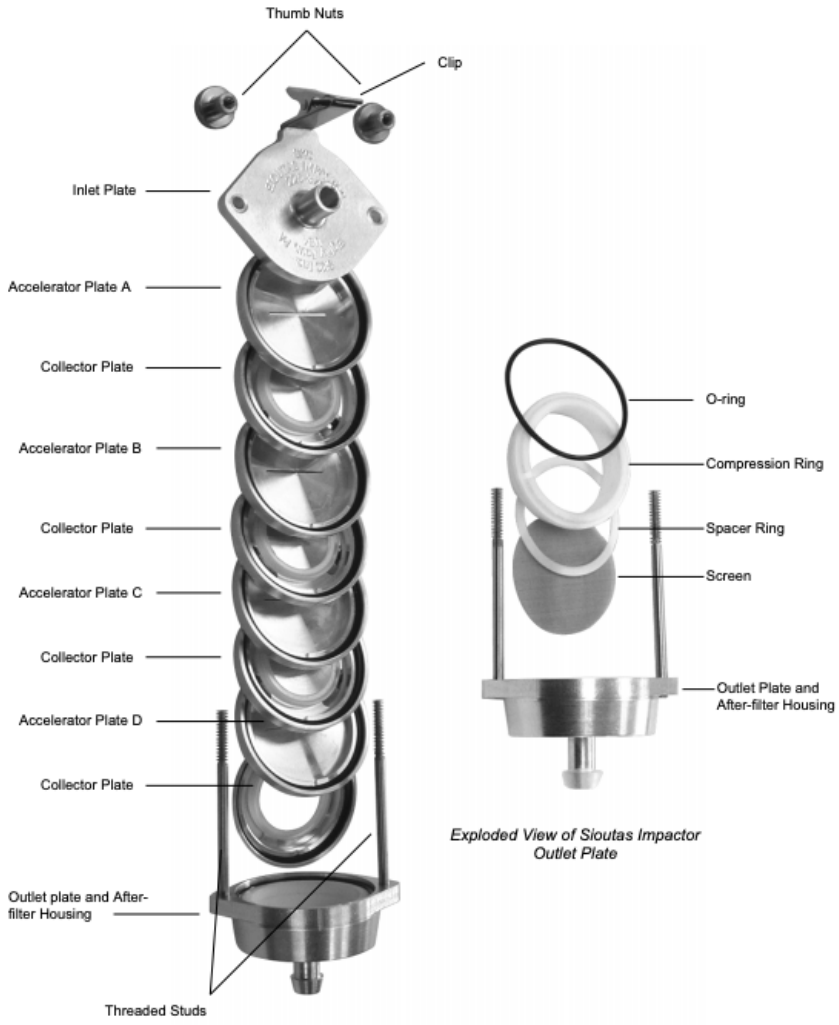

Figure I-5. Impactor, exploded view (adapted from Sioutas impactor brochure).

The National Center for Biotechnology Information (NCBI) gives the respirable aerosol limit as 10 μm AED. This is equal to a 3.02 μm (geometric) particle of UO_2.

The objective is to capture particles up to 10 μm AED to determine the respirable fraction. However, the off-the-shelf impactor does not provide a wide enough range of AED. According to Eq. (I-6), the impactor cut point can be adjusted by varying pump speeds or the cascade orifice dimensions. Both measures were adopted, and three additional stages were designed and added to the stack.

I-3.3 Cascade design modifications and calibration

Before the stages were designed, the miniature pumps that are used to provide flow to the sampler were tested by ORNL Metrology. The dedicated miniature pumps that are used for the impactors are powered by a battery pack. Because the batteries are not expected to provide constant voltage to the pumps, it was important to understand the flow rate as a function of elapsed time. However, the pumps are only expected to operate for about 15 minutes during aerosol collection. The cascade impactors (optimized for a flow rate of 9 LPM) are operated using one of the dual-head pumps that has a nominal design flow rate of 9.5 LPM. The drop-off in flow rate over time was also measured for one of each pump type and is

plotted in Figure I-6 for the dual-head pump. In all cases, the measured pump flow rate with fresh batteries was higher than the design-rated flow for the sampler, as listed in Table I-3. An in-line potentiometer was used to control the voltage and to dial in the desired flow rate for the test.

Table I-3. Measured pump flow rates for the Parker Dual Head pump (rated at 9.5 LPM).

Pump ID	Measured flow rate with fresh batteries (sccm)
PC-1	9,903
PC-2	9,948
PC-3	10,100
PC-4	9,986
PC-5	10,102
PC-6	10,122
PC-7	9,782
PC-8	9,944
PC-9	9,824
Average	9,997
Standard deviation	139

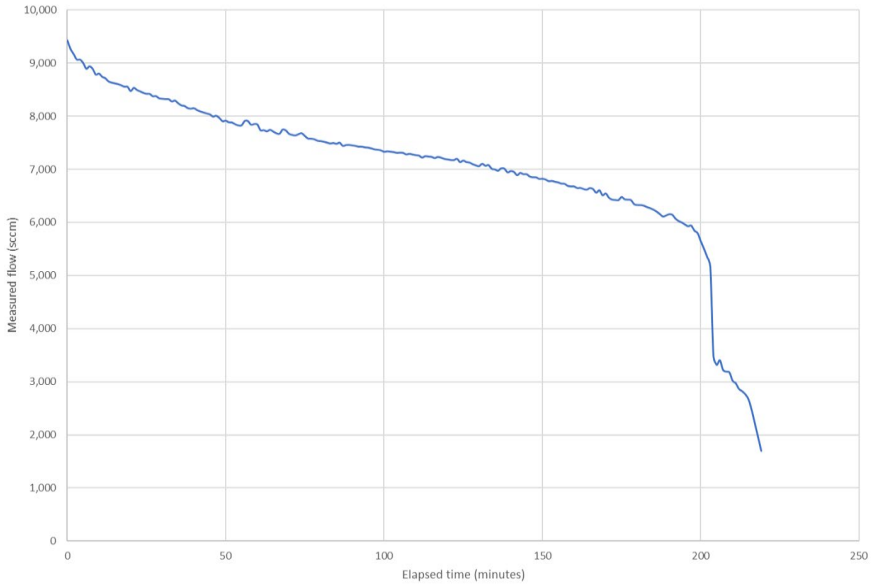

Figure I-6. Example of the change in dual-head pump output as a function of elapsed time.

A flow rate of 7 LPM was chosen to ensure that an appropriate rate was maintainable for the duration of the test and to achieve the desired cut-point distribution using the additional stages with the purchased stages. Table I-4 lists the new cut-off values for the purchased cascade using a flow rate of 7 LPM.

Table I-4. Cut points calculated for purchased impactor with measured dimensions at 7 LPM.

Stage	As-received cut point diameters (μm)	Equivalent UO_2 geometric diameter (μm)	As-received orifice width ± 0.0015 (cm)	As-received orifice length ± 0.0015 (cm)	Average Jet velocity (cm/s)
PA	4.11	1.241	0.102	2.007	569.0
PB	2.05	0.619	0.051	2.007	1140.0
PC	1.60	0.483	0.039	2.024	1452.0
PD	1.07	0.323	0.026	2.029	2169.0

To widen the cut point capacity of the cascade, three stages were added. The first stage is envisioned as a prefilter to collect the larger airborne particles that make it into the cascade. The orifice dimensions needed to achieve the desired cut points (15, 10, and 8 μm) at 7 LPM were specified by holding the length constant and optimizing the width as calculated using Eq. (I-6). The as-machined plates varied from the desired widths, and Table I-5 lists the as-built dimensions of the machined stages. The states were measured using a Leica S9i microscope, and the results were averaged from five readings, along with the cut-point values calculated for 7 LPM.

Table I-5. Post-machined dimensions of the added cascade stages and subsequent cut-point values.

Stage	As-built cut point diameters (μm)	Equivalent UO_2 geometric diameter (μm)	As-received orifice width ± 0.0015 (cm)	As-received orifice length ± 0.0015 (cm)	Average Jet velocity (cm/s)
MA	15.621	4.718	0.387	1.952	158.0
MB	11.637	3.515	0.288	1.919	218.0
MC	7.796	2.355	0.192	1.938	329.0

The final cascade configuration shown in Figure I-7 includes three machined stages, MA, MB, and MC, and four purchased stages, PA, PB, PC, and PD, stacked on extended lead screws in the cascade holder. The manufacturer recommends using a 25 mm polytetrafluoroethylene (PTFE) filter with 0.5 μm perforations; unfortunately, this material would disintegrate in the high radioactive environment anticipated in this experiment. Silver filters and carbon tabs were investigated as alternatives that would

Figure I-7. The orifice plates and stages of the modified Sioutas cascade impactor.

be amenable to SEM imaging and chemical digestion. However, the silver filters were rejected because the collected aerosol material can be easily dislodged, and it is anticipated that the cascades will be bumped around quite a bit in the hot cell. The carbon tabs are preferred because they can be used for SEM imaging and they have a sticky surface that will prevent adsorbed particles from reentering the air flow in the cascade.

I-4 Design Verification Using Physical Testing

Extensive testing of the modified cascade impactor was conducted to verify the calculated cut points. A powder dispenser was used to puff a known powder mixture into the collection system. After testing, the stages were disassembled, and the filters were analyzed. The collected particles were characterized using SEM. The image analysis steps adopted for characterizing and counting the particles are discussed in the next section. All validation tests were conducted using purchased International Organization of Standardization (ISO) dust mixtures that consisted of a number of compounds of varying density and particle sizes.

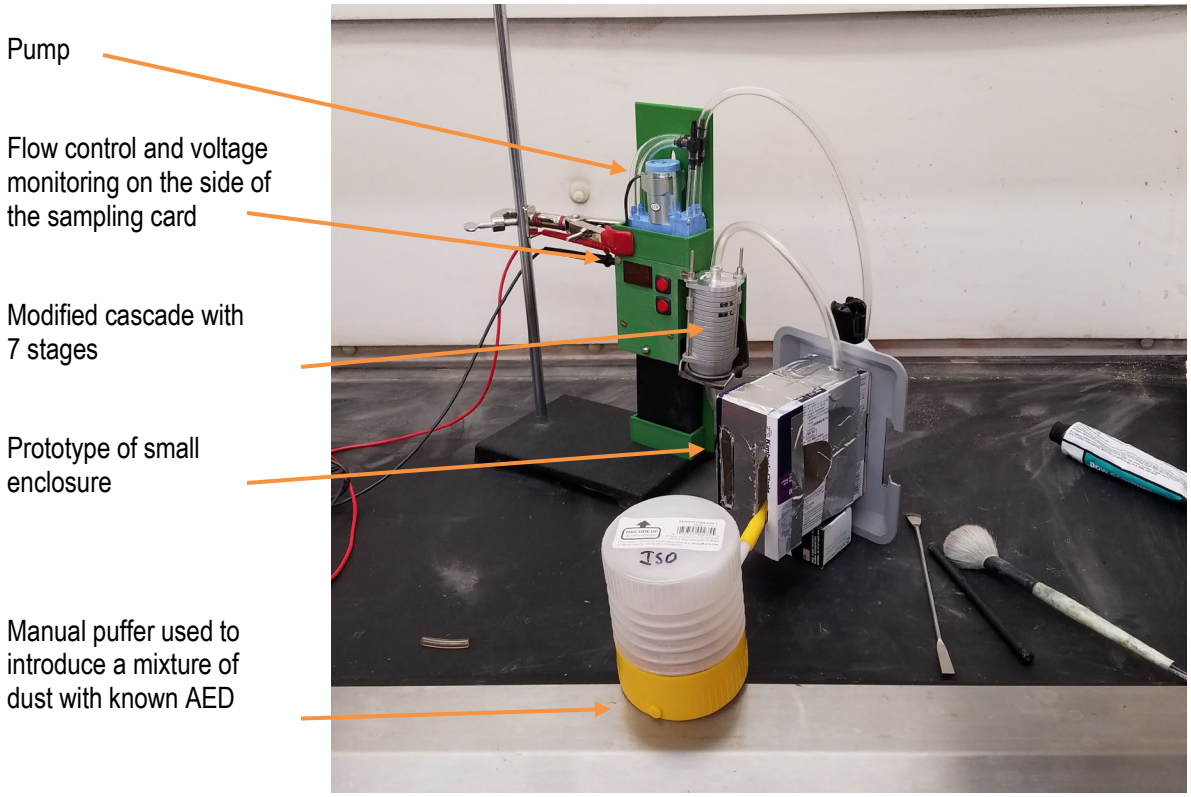

Figure I-8. Experimental setup for validation tests with the modified cascade and a prototype of the small enclosure.

Table I-6 lists the ISO dust concentration used for the tests. Several types of dust were used in testing: ISO 12103-1 A1 Ultrafine, A4 Coarse test dust, and CeO_2 powders of different particle sizes (3 µm, 5 µm & 14 µm). It was observed from SEM characterization that the CeO_2 powders had a smaller size

distribution than the rated particle sizes. Because the target aerosol collection size for the SNF rod tests is <10 μm in diameter, the ultrafine test dust is more representative of the diameters to be collected during the test, so it was used for the final verification tests. The composition and size distribution specification for the ultrafine test dust is provided in Table I-6.

Table I-6. Composition and particle size distribution of ultrafine ISO test dust.

Component	Quantity
Silica (fine dust)	69 – 77%
Aluminum oxide	8 – 14%
Calcium oxide (mineral)	2.5 – 5.5%
Potassium oxide (mineral)	2 – 5%
Sodium oxide (mineral)	1 – 4%
Iron (III) oxide (hematite)	4 – 7%
Magnesium oxide	1 – 2%
Titanium dioxide	0 – 1%

A1 ultrafine test dust particle size distribution by volume

Particle diameter (μm)	% less than
0.97	3.0 – 5.0
1.38	7.0 – 10.0
2.75	23.0 – 27.0
5.50	65.0 – 69.0
11.00	95.5 – 97.5
22.00	100.0

Several types of tests were performed, including:

- Pressure drop testing of individual stages and the assembled cascade
- Collection of various dust sources with the assembled modified cascade
- Collection of dust with varied stage order
- Collection of dust using various filter materials (paper, quartz, silver, carbon tabs [beige and black in coloration], no filter)
- Variation of the pump flow rate

For brevity, only select results from the tests performed are reported here, but all tests are documented in the experiment log book.

I-4.1 Pressure Drop Tests

Experimental pressure drop measurements were collected using a setup similar to that used for the verification testing (shown in Figure I-9), except that a flow meter and a pressure meter were included, as shown in Figure I-9. The vacuum pump was first turned on and adjusted to achieve the desired steady state flow rate. Experimental measurements were taken at each stage, along with overall pressure drops for the 7-stage Sioutas cascade impactor at inlet flow rates of 6 and 7 LPM. The first tests were conducted

using the full stack. Individual stage pressure drops were calculated by measuring the pressure drop across the stack without that stage and then subtracting the minus-one measurement from the full stack measurement. An alternative measurement technique of successively removing the stages (first 1, then 2, then 3, etc) produced similar pressure drops for the individual stages. The results are provided in Table I-7 and are used in conjunction with the computational fluid dynamics (CFD) models to verify expected performance with the modified stages.

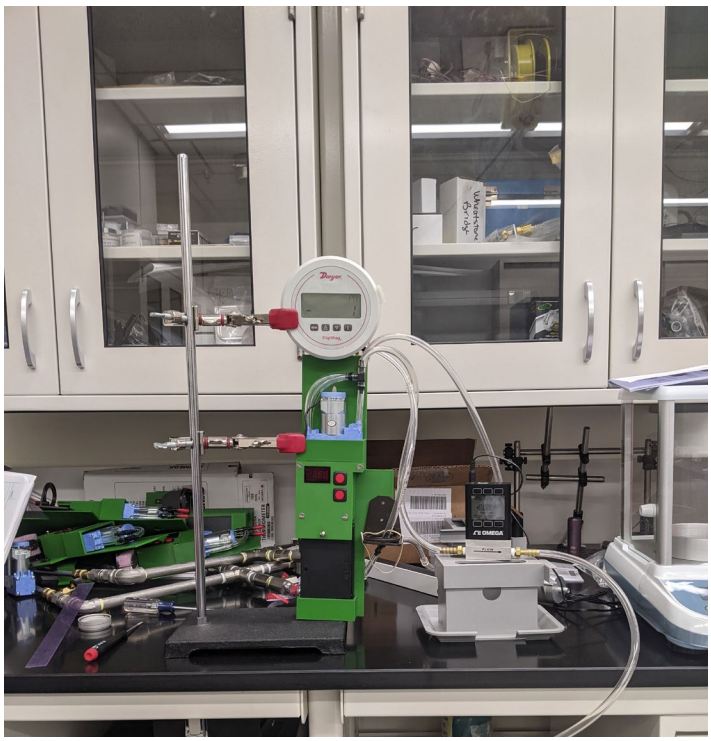

Figure I-9. Experimental test setup of the 7-stage modified Sioutas cascade impactor with flowmeter and the pressure transducer.

Table I-7. Experimentally measured pressure drop values for the modified Sioutas cascade impactor at 6 and 7 LPM.

Impaction stage	Measured ΔP at 7 LPM (Pa)	Measured ΔP at 6 LPM (Pa)
Stage MA	0	0
Stage MB	0	0
Stage MC	30 ± 30	18 ± 30
Stage PA	62 ± 30	25 ± 30
Stage PB	128 ± 30	99 ± 30
Stage PC	220 ± 30	178 ± 30
Stage PD	675 ± 30	481 ± 30
Overall	1,156	867

I-4.2 Collection Efficiency Verification

Multiple tests were performed using ISO dust mixtures and ceria powders to examine the collection efficiency of the modified Sioutas cascade using the setup shown in Figure I-9. The surrogate dust deposits were weighed, imaged (see Figure I-10 for a photographic example), and analyzed. The performance of the modified cascade was within expectations.

The assembled order of the stages was changed to evaluate individual stage efficiency (no collection on stages with a higher cut point placed below a lower cut point stage). The filters were weighed pre- and post-collection to determine the amount of powder collected. In the test results shown in Figure I-11, the deposited material from filter MB was dislodged and lost as a result of the handling process. This highlighted the fact that sticky carbon tabs, as shown in Figure I-12, were more efficient in retaining particles deposited on the stage and preventing loss through handling. SEM samples were taken from each filter for evaluation. Each sample was collected from the center and sides of the filter to check for a change in distribution along the air flow path.

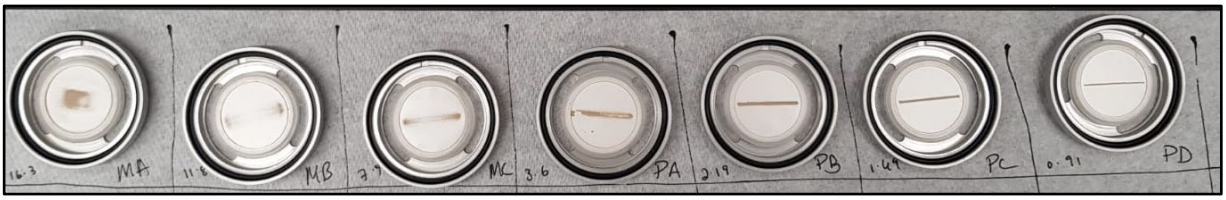

Figure I-10. Silver filters imaged after validation experiments with ISO dust.

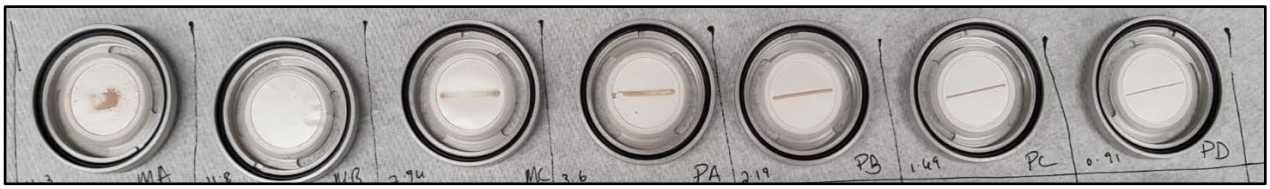

Figure I-11. Silver filters imaged after weighing. The filter MB material deposit was lost during the weighing process.

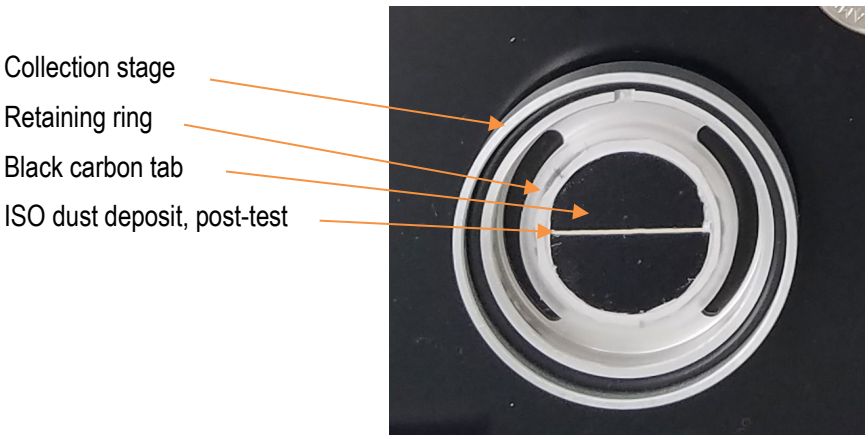

Figure I-12. A black carbon tab used to collect ISO particle samples. In the hot cell, a beige-colored tab will be used to allow for visual identification of UO_2 deposits.

To evaluate the individual stages, the stack was arranged out of order as MB, MC, MA, PA, PB, PC, and PD, and ISO dust was puffed into the collection box. Figure I-13 shows the filters with the collected ISO dust particles from this run. It was observed that filter MA showed no collection compared to that of MB, MC, and the purchased stages. This produced the expected result: MB and MC collected all the larger particles from the air stream, but they left behind smaller particles. There were no larger particles remaining for deposit on MA, and, as a result, it was empty.

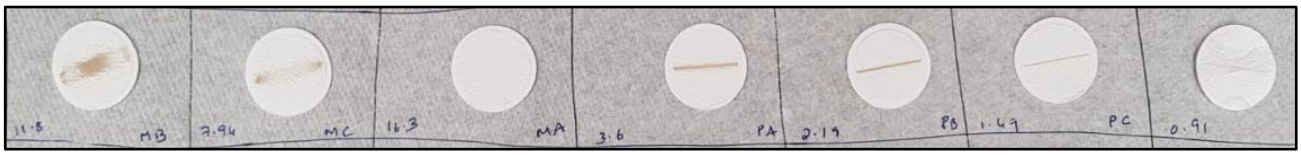

Figure I-13. The out-of-order placement of MA below MB and MC produced no deposits on MA, as expected, because the larger particles were already removed in the stages above it (quartz filters).

All tests with the ISO dust resulted in deposits on the orifice plate, in addition to the collection plate, as shown in Figure I-15. The amount varied, depending on the volume of dust introduced for the test. It is unlikely that a large amount of SNF dust will be deposited on the orifice plates, because the volume of SNF dust is expected to be small compared to that used in the ISO dust tests; nevertheless, sampling should include the orifice plates.

Figure I-14. Typical ISO dust deposit on the orifice plate's surface.

I-4.3 SEM Image Processing

Verifying distribution of the particle sizes deposited on each stage requires an image of the deposits and a method for counting and measuring each particle. For particles the size of aerosols, imaging capable of resolving each particle requires SEM. Representative images of the deposited material on each stage of the cascade can be acquired using the IFEL's SEM. With confidence in the capabilities of the cascade, imaging and image processing are not strictly required; however, the additional evidence provided by the images is considered extremely useful and relevant. Image processing tools are available, but the type of image acquired in this test (many small particles in a pile) is very difficult to process reliably. Also, only the visible particles can be characterized, and those below the top layer are ignored. Therefore, image processing cannot provide a complete tool to evaluate the resulting material collection on the various cascade stages, but it can provide verification that the visible particles fit the expected distribution. A literature review was completed, and existing tools in MATLAB [I-13 through I-18] and IMAGEJ Fiji [I-19] were selected for use.

To verify the counting and measurement process, samples from the ISO dust test were evaluated. A MATLAB script 'Count_Measure_Blobs' was employed to count the collected aerosol particles from the SEM images. The script converts images to grayscale before setting a threshold based on the highest pixel count, and it also connects the pixels around a specific, central pixel to identify individual particle regions. The regions are then combined to generate a labeled binary image before being counted. The *regionprops* function is then used to obtain the mean pixel intensity, area, perimeter, centroid, and diameter of particles (blobs) in the region. Further information on the script and methods can be found on the Mathworks website's Image Analysis toolbox [I-13].

Table I-8 gives the percentage of particles collected across MA, MB, MC, PA and PB for the different particle sizes in ISO dust, as counted by the MATLAB script. The first three stages (the added stages) collected most of the large particles, but they also picked up smaller particles that appear to be adhered to the large particles. This is likely the result of agglomeration from humidity. It was also noted that the lower four stages (the as-received purchased cascade stages) did not pick up any of the large particles and thus follow the designed cut point trends at 7 LPM. Unfortunately, stages PC and PD were omitted from this analysis as the particles were highly agglomerated and the MATLAB script was picking up agglomerated particles as giant blobs as seen in Figure I-17 and Figure I-18.

The unusually high number of smaller particles (0–1.5 μm) and agglomerated particles picked up by the first three stages prompted a more detailed examination of the particle counting techniques used in this study. Several errors were observed when the procedure was used directly without pre-processing the SEM image. The errors were related to over estimation and misrepresentation of agglomerated and low-contrast particles as separate or combined blobs, as illustrated in Figure I-15, Figure I-16, and Figure I-17. Figure I-16 shows a high magnification image of the filter from stage MA, with ISO dust collection along with the labeled image from the MATLAB script. The error shown resulted from cracks and crevices in large particles, which led to a break in the pixel connectivity. This caused the script to identify multiple miniscule particles instead of one single large particle.

Table I-8. Percentage of ISO dust particles collected across various size groups for the 7 stages at 7 LPM, counted with the MATLAB script without preprocessing.

Distribution (μm)	MA %	MB %	MC %	PA %	PB %
0–0.5	15	0	19	0	67
0.5–1	29	38	12	8	13
1–1.5	13	33	30	0	25
1.5–2	22	22	13	22	22
2–2.5	13	26	23	28	10
2.5–3	18	22	10	38	12
3–3.5	26	21	12	38	3
3.5–4	29	18	26	24	3
4–4.5	44	15	22	19	0
4.5–5	33	33	26	7	0
5–5.5	26	9	65	0	0
5.5–6	50	22	28	0	0
6–6.5	31	6	56	6	0
6.5–7	54	0	46	0	0
7–7.5	30	10	60	0	0
7.5–8	67	0	33	0	0
8–8.5	75	0	25	0	0
>8.5	43	19	38	0	0

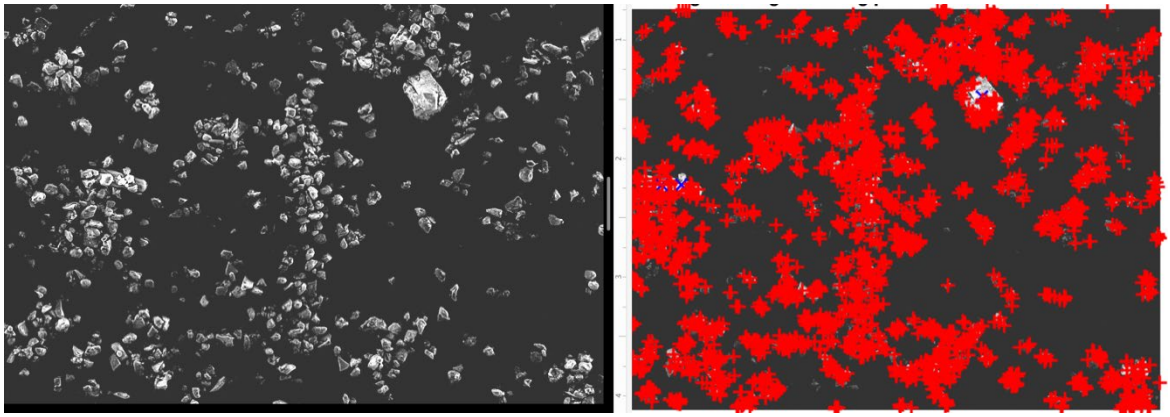

Figure I-15. SEM image of MA filter with ISO dust and the particle count outcome from the MATLAB script showing overestimation of particles caused by poor thresholding.

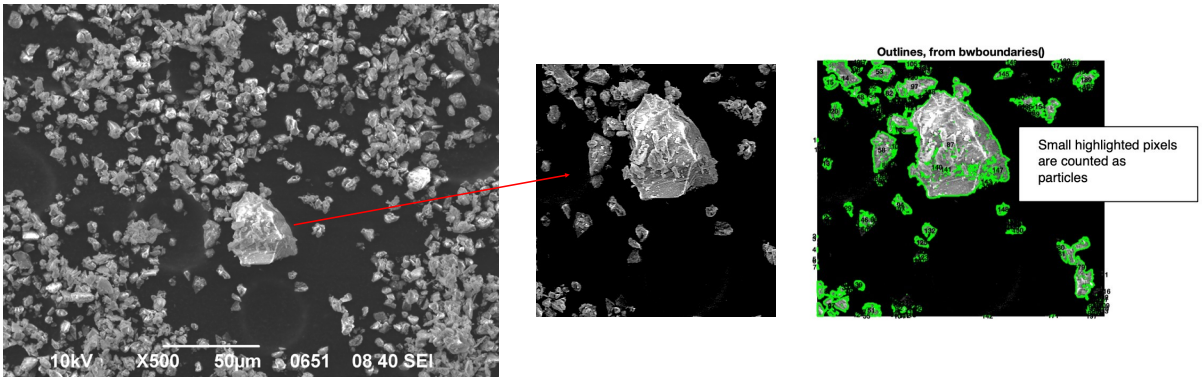

Figure I-16. High magnification SEM image of MA filter with ISO dust and the particle count outcome from the MATLAB script showing separate particles being identified in a large particle with minor contrast variations within the region.

Figure I-17 shows a high magnification image of filter MC with ISO dust collection, along with the binary image outcome from the MATLAB script image processing steps. It can be seen that agglomerated particles with low boundary resolution are counted as giant particles, thus leading to misrepresentation of the particle ranges collected.

Several approaches were tried to rectify these problems, including sophisticated thresholding techniques (Ostu [I-14]), segmenting the image into smaller images and recombining (adaptive thresholding and binarization [I-15]), finding edges before binarizing [I-16], using different structuring element functions for reconstruction (opening and closing) to distinguish particle edges before counting [I-17], and watershed segmentation [I-18]. Furthermore, the images were also preprocessed using ImageJ and Fiji software before counting.

For this application, the best approach was found to be using the Trainable Weka Segmentation [I-19], a machine learning tool in Fiji for preprocessing images before counting the particles using the MATLAB script with Ostu's thresholding approach.

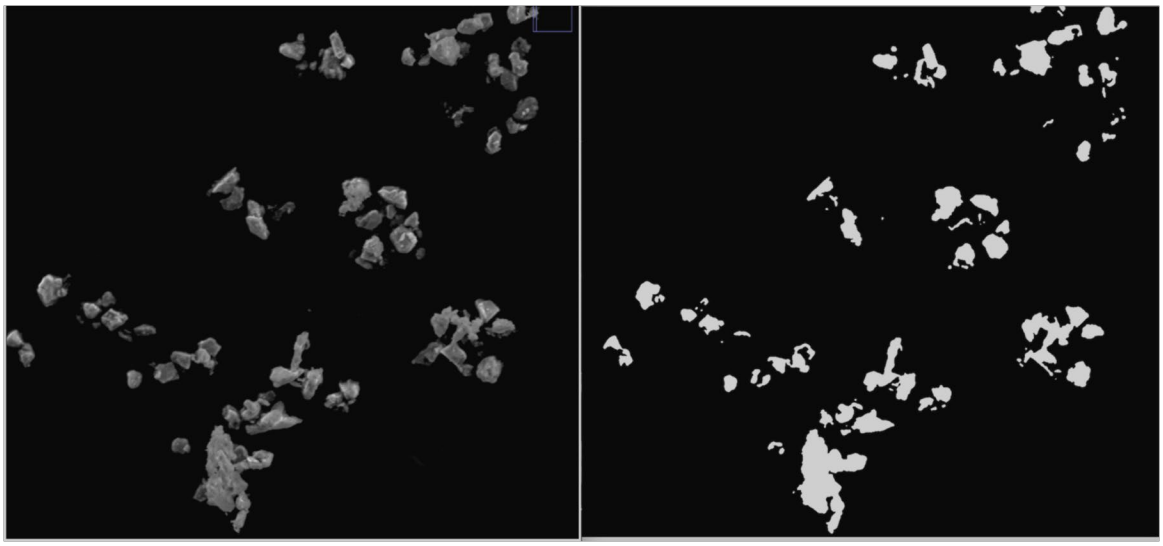

Figure I-17. High magnification SEM image of MC filter with ISO dust and the binary image generated by the MATLAB script showing small particles with low pixel intensity variations merged into one large blob.

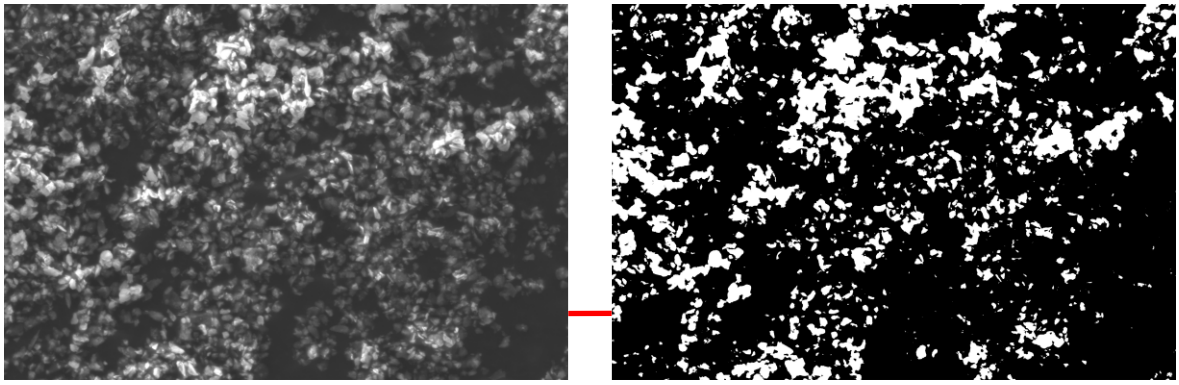

a) b)

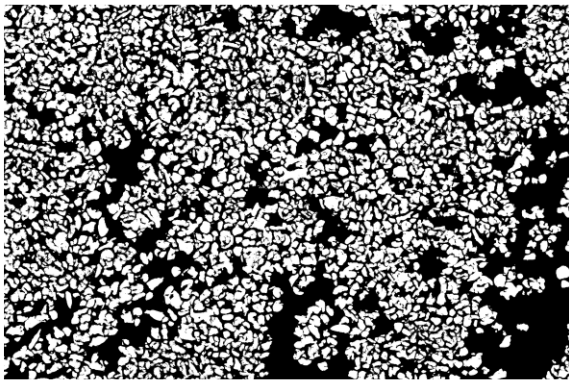

c)

Figure I-18. (a) SEM image of PC filter with ISO dust, (b) binary image output of (a) from the MATLAB script without preprocessing, and (c) trainable Weka segmented image after binarization showing a very effective approach for identifying and isolating particles.

These techniques were used, and the filters were re-analyzed to obtain the percentage of particles collected for the different particle sizes in ISO dust as counted by the MATLAB script. The data are presented in Table I-9. Using this processing technique, stages PB, PC, and PD collected most of the smaller particles between 0.1–1.5 µm, and the machined stages collected very few particles in this size range. MA has a wide range of collection. Stage PA collection is low compared to the other stages.

Validation of the modified Sioutas cascade performance through image analysis is ongoing, with active investigation of improvements in the counting scripts and image preprocessing. Further validation of the machined stages and the cascade impactor was performed computationally by modeling the impactor and conducting fluid dynamics simulations to analyze the trends observed in the processed image data.

Table I-9. Percentage of ISO dust particles collected across various size groups of ISO dust powders for the 7 stages at 7 LPM, as counted using the MATLAB script after preprocessing the SEM images.

Distribution (µm)	% MA	% MB	% MC	% PA	% PB	% PC	% PD
0–0.5	1	6	7	3	24	28	32
0.5–1	11	19	16	5	0	21	28
1–1.5	14	11	11	4	49	4	8
1.5–2	6	14	10	6	50	10	4
2–2.5	13	26	11	7	37	0	7
2.5–3	4	33	17	8	29	8	0
3–3.5	7	60	13	20	0	0	0
3.5–4	19	38	19	13	13	0	0
4–4.5	29	33	24	10	5	0	0
4.5–5	20	50	20	0	10	0	0
5–5.5	7	21	36	7	29	0	0
5.5–6	33	44	22	0	0	0	0
6–6.5	25	25	25	15	0	0	0
6.5–7	25	25	25	7	0	0	0
>7	53	13	27	5	0	0	0

I-5 Design Verification Using Computational Fluid Dynamics Tools

The flow distribution and particle deposition on the cascade impactor were investigated using the commercial computational fluid dynamics (CFD) code, STAR-CCM+ (Version 2021.1 Build 16.02.008) from Siemens [I-20], an American Society of Mechanical Engineers (ASME) Nuclear Quality Assurance (NQA-1)–compliant CFD solver. STAR-CCM+ has been extensively benchmarked and applied to various areas, including multiphase flows, external aerodynamics, reacting flow networks, and treatment of complex geometric shapes. STAR-CCM+ uses a finite-volume formulation to solve a set of conservation equations for mass, momentum, and energy, along with models that provide closure to the Reynolds-Averaged Navier-Stokes (RANS) equations describing turbulent flow on a finely discretized computational grid. The CFD simulations discussed here are run on high-performance computing (HPC) resources hosted by ORNL's Nuclear Energy and Fuel Cycle Division (NEFCD).

As a starting point, the commercially available Sioutas cascade was modeled and used to verify the simulation's basic functionality. This initial simulation used the manufacturer's recommended inlet flow rate of 9 LPM. The model was then extended to the modified 7-stage impactor. The 3D geometry of the 4-stage cascade impactor is shown in Figure I-20. Only the fluid domain shown in Figure I-20(b) is modeled; the solid–fluid interfaces are modeled as walls. The flow direction is from left to right, with the gravitational vector in the positive y-direction. In an actual test, a vacuum pump will be operated (shown in Figure I-2) with the suction side at the outlet and the induction side at the inlet of the cascade impactor.

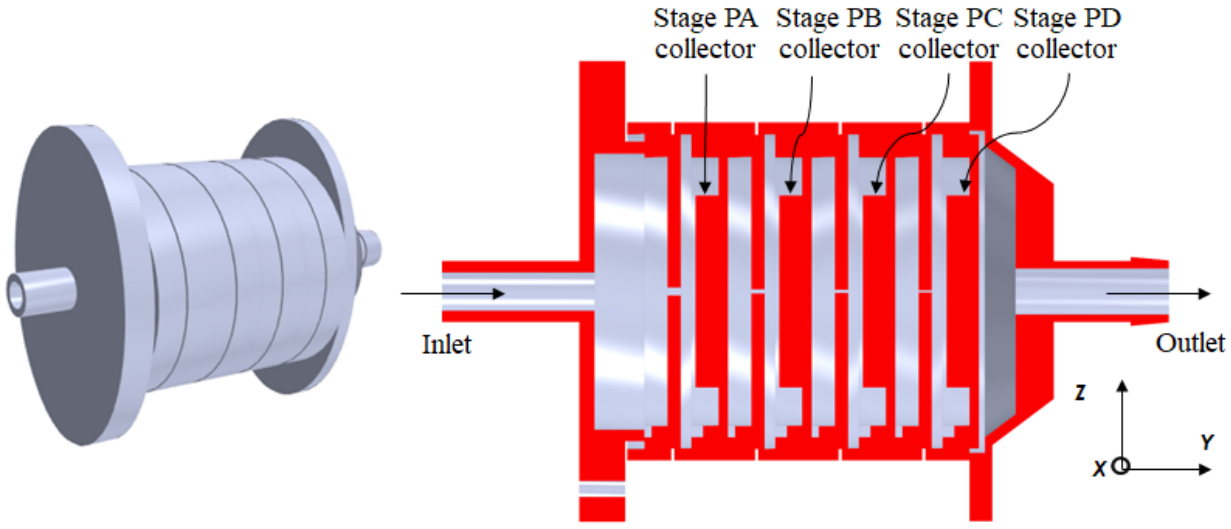

Figure I-19. (a) Isometric view of the Cascade impactor showing all 4 stages, including inlet and outlet plates; (b) a cross sectional view of the impactor with the solid domain shown in red and the fluid domain shown in gray.

In the model, the long, flexible tubing in the experimental setup was replaced by a rigid pipe geometry which is adequately extended to ensure a fully developed flow at the inlet of the cascade impactor over the range of simulated Reynolds numbers. The dimensions of the orifices for the 4 stages used in the CFD model were based on microscopic measurements, as discussed in Section I-3.2. An example of one such measurement (X-Z plane) of the orifice width for stage PD at various locations is shown in Figure I-21. The mean measured orifice widths for all 4 stages are listed in Table I-10. The separation distance, S, is defined as the distance between the orifice exit and the impaction plate. Although the specifications for the first three stages match well with the reference specification [I-5], there is a considerable difference in stage PD measurements for orifice width and length. The CFD model is based on the microscopic measurements, given that the stage pressure drop in particular, is very sensitive to the orifice dimensions.

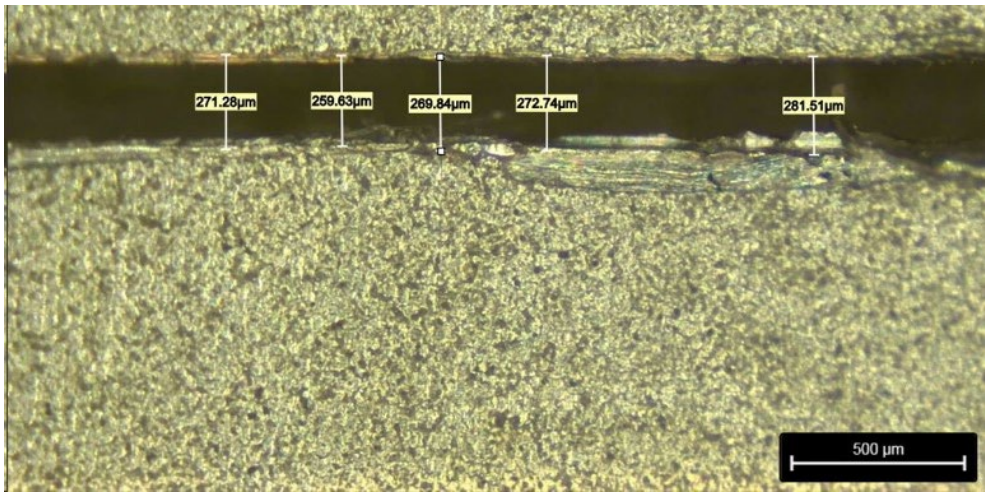

Figure I-20. Microscope measurement of Stage PD orifice width taken at various locations. The average Stage PD orifice width is 0.265 ± 0.015 mm

Table I-10. Measurements for the 4 stages using a microscope (CFD) compared to the manufacturer's specifications.

Impaction STAGE	Orifice width [I-5], mm	Orifice length [I-5], mm	Separation Distance to Orifice Width (S/W) [I-5]	Measured width, mm ± 0.015 mm	Measured length, mm ± 0.015 mm	Modeled S/W
Stage PA	0.9	19.0	2.10	1.022	20.070	1.85
Stage PB	0.5	21.0	3.78	0.51	20.070	3.69
Stage PC	0.36	19.0	5.25	0.397	20.245	4.76
Stage PD	0.14	25.0	13.50	0.265	20.295	7.13

Only half of the cascade sampler was modeled because the single-phase flow distribution is expected to be symmetric about the Y-Z (X=0) plane, which divides the flow geometry into equal halves. The coupled solver was used to solve for the continuity and momentum equations without solving for the energy equation. Because these tests are conducted at room temperature at low Mach numbers, the energy equation was ignored. Air with constant material properties was used at atmospheric system pressure. The shear stress transport (SST) k-ω model with an all y+ wall treatment was selected to model turbulence. Second-order numerics were used for spatial discretization for both the coupled and turbulence solvers. The flow in the domain switches between transitional turbulent to laminar flow. Tests with a transition turbulence model showed less than 2% change in the predicted stage and overall pressure drops, and produced a similar flow distribution, in comparison to the test without a transition model (base model). The flow remains turbulent for all inlet conditions. Therefore, it was decided that the base turbulence model was adequate.

The flow distribution tests were all performed for a steady-state condition. The velocity inlet boundary condition (BC) was used for the inlet boundary, and the outlet BC was used for the outlet boundary. The no-slip BC was used for all walls, and the symmetry BC was used for the symmetry plane. A block-

structured mesh was generated in STAR-CCM+ with a total mesh count of ~3.16 million. The block-structured (hex) mesh strategy was used to minimize computational cost and to adequately resolve the regions of interest. Four prism layers were used to capture the boundary layer, with the wall y+ less than one for the majority of the domain. The mesh settings listed in Table I-11 were used for the simulations.

Table I-11. Mesh settings for the trimmer and surface remesher models.

Meshing tool	Trimmer
Base size	5.0e-4 m
Surface growth rate	1.3
Number of Prism layers	4.0
Prism layer thickness	4.5e-5 m
Stage-1 Notch custom size	1.75e-4 m
Stage-2 Notch custom size	1.5e-4 m
Stage-3 Notch custom size	1.0e-4 m
Stage-4 Notch custom size	5.0e-5 m
Total number of cells	3.17e6

A mesh snapshot of the computational domain is shown in Figure I-22(a), and a close-up view of the refined mesh in the region of the orifices and the collectors is shown in Figure I-22(b). The mesh was refined in the orifice and collector regions because the solutions showed that the gradients of pressure and velocity are high in that region. Almost all of the pressure drop and flow acceleration occur as the flow enters the orifice. Similarly, the collector region is also important because it has a direct bearing on the particle collection dynamics. A mesh refinement study was conducted with the highest flow rate (9 LPM),

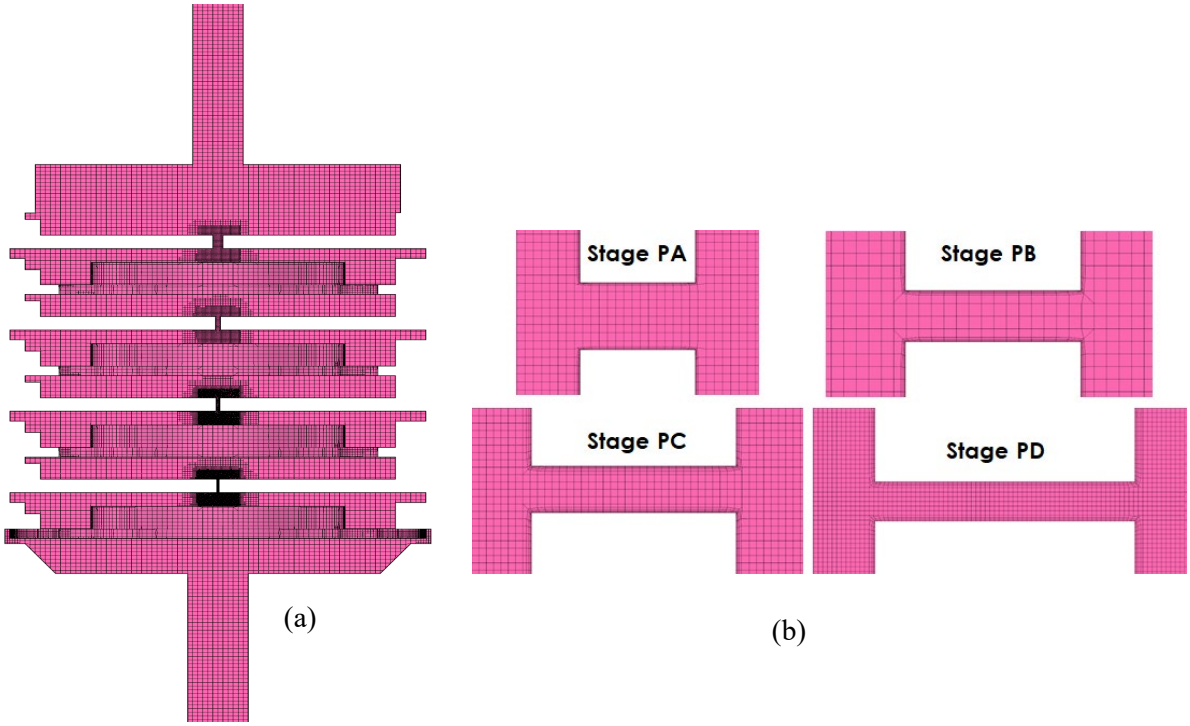

Figure I-21. (a) Slice through the computational grid on the symmetry (x = 0) plane; (b) close-up of the finely meshed orifice region for the 4 stages.

by halving the base size in Table I-11. The mesh was shown to be converged, since the difference in predicted stage-wise and overall pressure drop between the two meshes was within 1%.

I-5.1 Steady State Simulations

All steady-state simulations were performed using 64 processors with a total runtime of approximately 1 day. The solution was deemed to be converged when residuals (continuity, momentum, and turbulence) dropped by approximately three orders of magnitude, starting from the initial conditions summarized in Table I-12.

Table I-12. Initial conditions for the steady-state 4-stage cascade impactor simulation.

Pressure	1 atm
Velocity	0 m/s
Turbulence velocity scale	1.0 m/s
Turbulence intensity	0.01
Turbulence viscosity ratio	10.0

Furthermore, negligible changes were obtained in the selected monitor points: velocity magnitude monitor points in the nozzles, pressure and turbulence intensity at the outlet boundary, and maximum y+ of all wall surfaces in the domain. Results of the 4-stage cascade impactor for an inlet flow rate of 9 LPM are shown in Figure I-23, Figure I-24, and Figure I-25.

The velocity contour plot in two Y-Z planes is provided in Figure I-23, and the corresponding streamline plot showing the flow distribution in the entire domain is provided in Figure I-24. Three observations can be made regarding flow results:

1. The flow accelerates as it enters the orifices and the majority of the pressure drop also occurs in this region.
2. The velocity magnitude in the remaining parts of the domain are negligible, and low-magnitude recirculation patterns can be seen in various parts of the domain, such as the inlet region before stage PA.
3. The flow through the orifice in stage PA has a sharp gradient in the X-direction (see Figure I-23(b)) because the flow exiting the inlet pipe section does not pass through a header. Furthermore, the flow exits the orifice with a similar velocity profile because of a short orifice flow development length. This has implications for the predicted particle depositions, as discussed in the next section.

Contours of (static) pressure are shown in Figure I-25 at two Y-Z planes. Significant pressure drop is shown to occur at the entrance of each of the orifices, with the maximum pressure drop observed for stage PD. A small rise in pressure is seen at the stagnation point. The predicted pressure drops from the simulation (CFD) across each of the 4-stages are compared to manufacturer-reported values [I-5] in Table I-13, where Re_W is the Reynolds number defined with respect to the orifice width and Re_{Dh} is the Reynolds number defined with respect to the hydraulic diameter of the orifice.. The uncertainty of the predicted values is calculated using Eq. I-9.

The predicted average/area-averaged velocity and the manufacturer-listed values differ because of variations between the model (measured) and the manufacturer's orifice dimensions. The Reynolds number for the model, based on the orifice hydraulic diameter D_h, is also listed. It can be observed that the Re_{Dh} values spanning the laminar/transitional regime are fairly consistent across the four orifices. The error between the manufacturer's specified pressure drops and the CFD-predicted pressure drops

decrease from stage PA to stage PD. Given the sensitivity of the pressure drop to the notch dimension, the differences could be due to manufacturing variability. Additionally, the manufacturer's measurements also include measurement uncertainty [I-5]. In general, the model predicts a higher pressure drop for a given dynamic head when comparing the manufacturer's mean velocity (U_{avg}) with the model-predicted mean velocity, where the mean is defined as

$$U_{avg} = \frac{\int \rho u(x,y,z) dA_c}{\rho dA_c}, \tag{I-9}$$

where ρ is the (constant) air density, A_c is the cross-sectional area of the orifice, and u is the local velocity magnitude. The pressure drop was also measured for the 7-stage cascade impactor at inlet flow rates of 6 and 7 LPM, as described in Section I-4.1, and the measured values are compared with those predicted by the model in Table I-13.

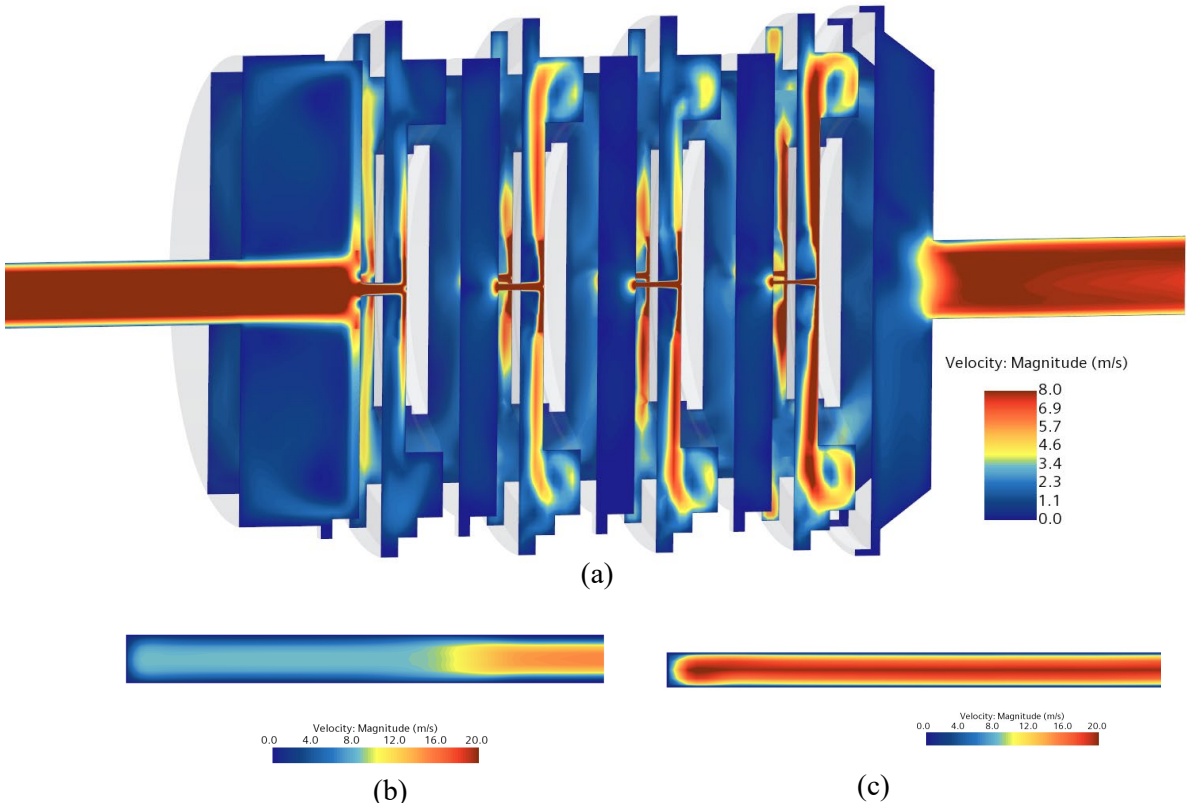

Figure I-22. (a) Contours of velocity magnitude (9 LPM) on x = 0 plane and x = -8 mm plane, (b) velocity magnitude contour (y=0) at a midplane on the orifice stage PA, (c) Velocity magnitude contour (y=0) at a midplane on the orifice stage PB.

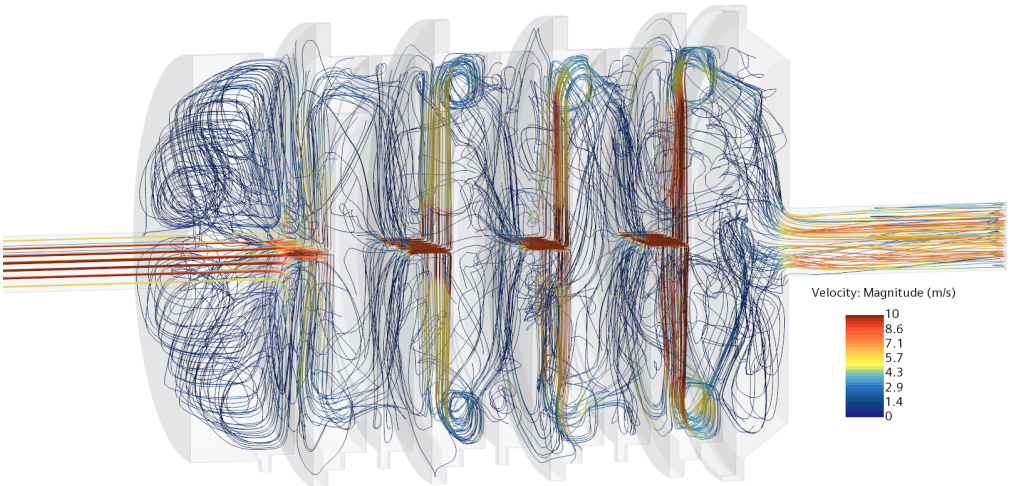

Figure I-23. Streamline plot of the flow distribution through the 4-stage cascade impactor colored according to velocity magnitude (9 LPM).

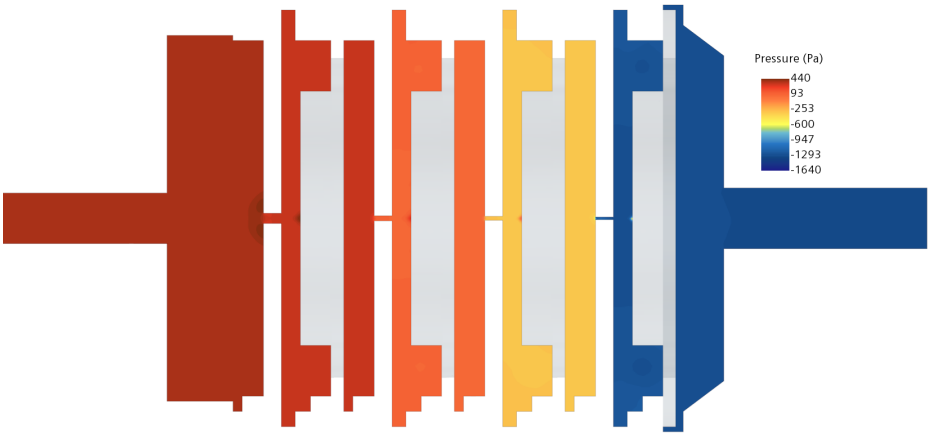

(a)

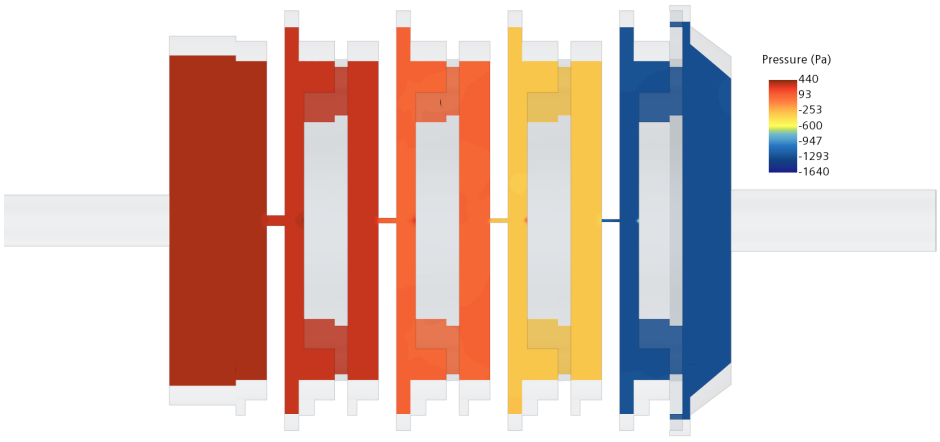

(b)

Figure I-24. Pressure contours (9 LPM) on (a) x = 0 plane and (b) x = -8 mm plane.

Table I-13. Comparison of model predictions and manufacturer's specifications for the 4-stage cascade impactor at 9 LPM.

	Manufacturer's specification [I-5]			CFD-predicted			
Impaction stage	U_{avg}, m/s	Re_W	ΔP, Pa	U_{avg}, m/s	Re_W	Re_{Dh}	ΔP, Pa
Stage PA	8.77	473.7	75	7.47	487.0	956.0	42 ± 1
Stage PB	14.29	428.6	149	14.67	477.5	960.5	249 ± 15
Stage PC	26.32	473.7	373	18.70	473.9	929.7	408 ± 29
Stage PD	42.86	360.0	971	27.92	472.3	932.4	947 ± 100

The geometric parameters used to model the 7-stage cascade impactor, which includes three additional machined stages (MA, MB, MC), are listed in Table I-14.

Table I-14. Geometric parameters modeled in the 7-stage cascade impactor.

Impaction stage	Orifice width mm ± 0.015 mm	Orifice length, mm ± 0.015 mm	S/W
Stage MA	3.87	19.525	0.49
Stage MB	2.883	19.190	0.66
Stage MC	1.923	19.385	0.98
Stage PA	1.022	20.070	1.85
Stage PB	0.51	20.070	3.69
Stage PC	0.397	20.245	4.76
Stage PD	0.265	20.295	7.13

As in the 4-stage impactor model, symmetry was used, and only one-half of the geometry was modeled, because the flow distribution is expected to be symmetric about the Y-Z plane. The BCs and solver models chosen for this study were similar to those used in the 4-stage impactor simulation, with the coupled solver used for the continuity and momentum equations, and the SST k-ω model used for turbulence. A block structured mesh was generated in STAR-CCM+, with a total mesh count of ~3.87 million. A mesh snapshot of the 7-stage impactor model is shown in Figure I-25.

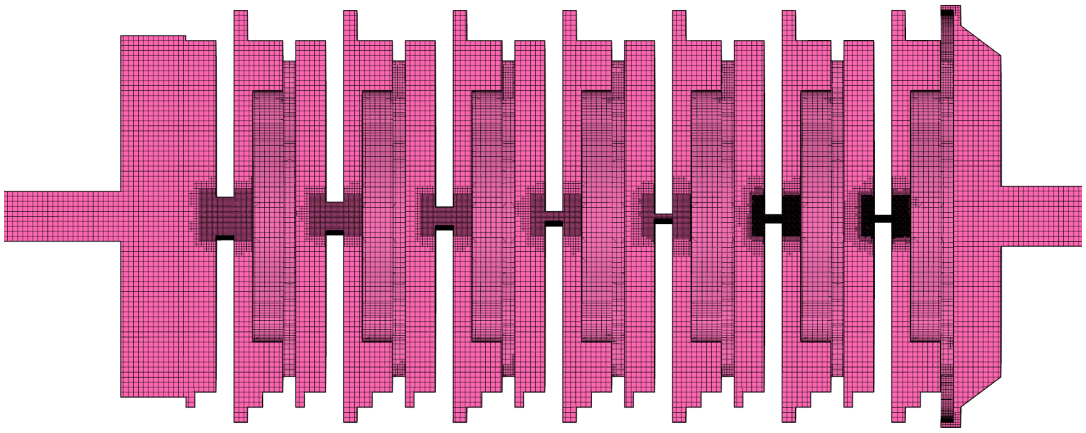

Figure I-25. Slice through the computational grid on the symmetry (x = 0) plane for the 7-stage cascade impactor model.

All simulations for the 7-stage cascade were performed using 64 processors, with a total runtime of approximately 1 day. Convergence criteria similar to those used for 4-stage impactor model were used for the current model. The results of the 7-stage cascade impactor for an inlet flow rate of 7 LPM are shown in Figure I-27 through Figure I-29. The velocity contour plot in two Y-Z planes are shown in Figure I-27, the velocity magnitude in the seven orifices about a X-Z mid-plane is shown in Figure I-27, and a streamline plot showing the flow distribution in the entire domain is shown in Figure I-28. Similar conclusions can be drawn for the 7-stage impactor and the 4-stage impactor. The core peaked velocity profile is more pronounced for the flow in the orifice of stage MA. Unlike with the 4-stage impactor study, the flow in stage PA in the 7-stage impactor study is similar to the flow distribution in the downstream orifices, because the flow entering the orifice of stage PA is well distributed, unlike in the 4-stage cascade. The pressure contour at two Y-Z planes is shown in Figure I-29. As in the 4-stage impactor study, significant pressure drops are observed in the orifice inlets. Relatively negligible pressure drops

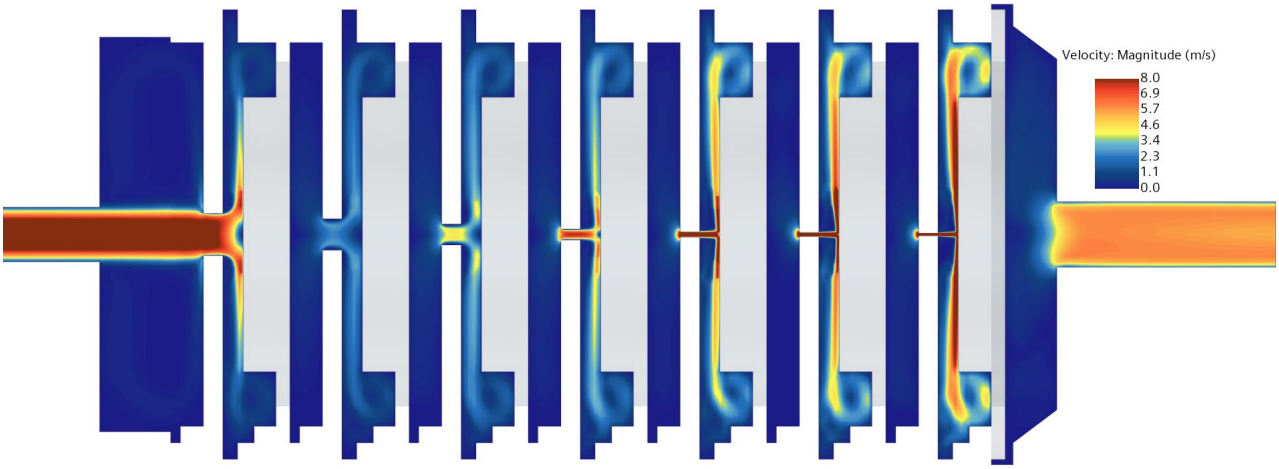

(a)

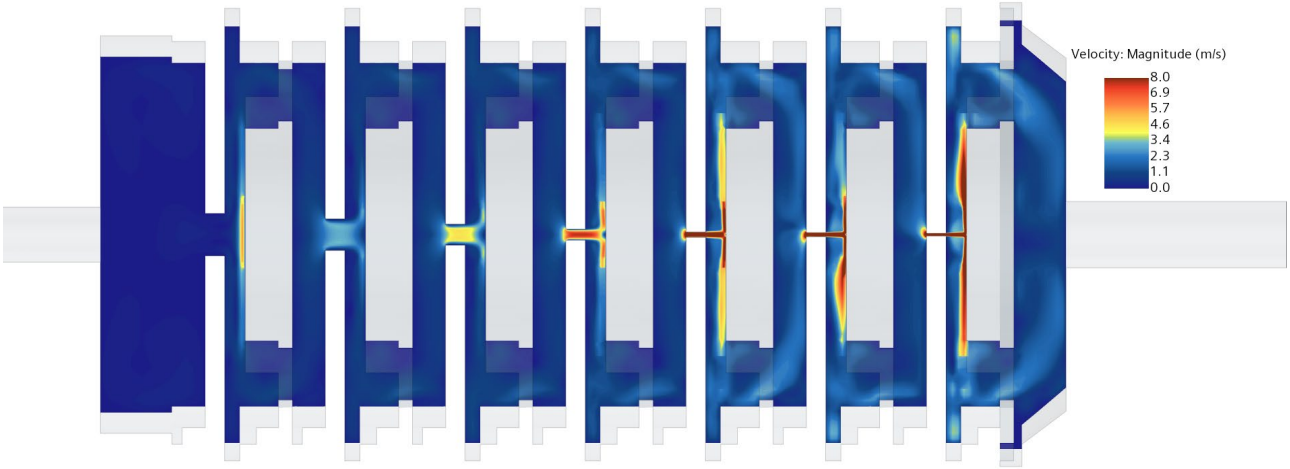

(b)

Figure I-26. Contours of velocity magnitude (7 LPM) for the 7-stage cascade impactor on (a) x = 0 plane and (b) x = -8 mm plane.

were observed at the orifice entrance for the three added stages, and the average flow velocities were lower in comparison to stages PA-PD.

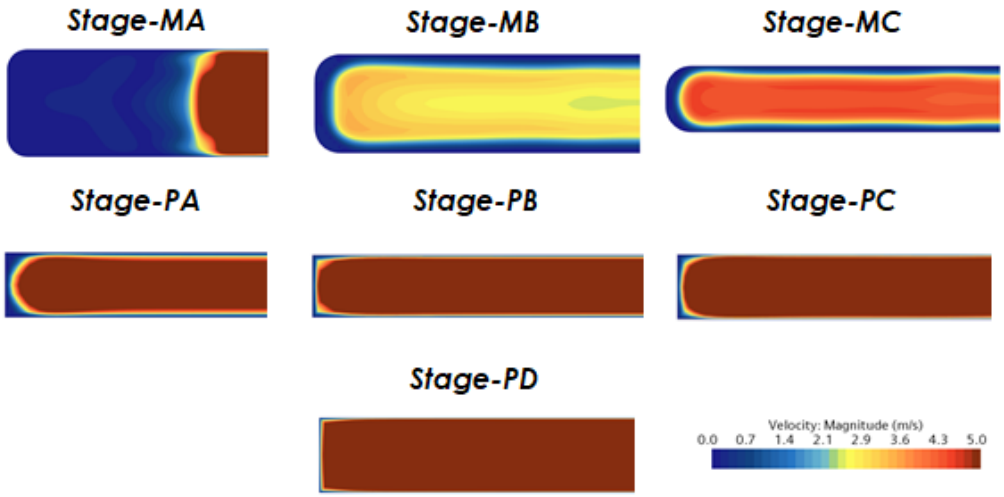

Figure I-27. Orifice velocity magnitude contour (y=0) at the midplane (half of the orifices are shown) for the 7-stage cascade impactor at 7 LPM.

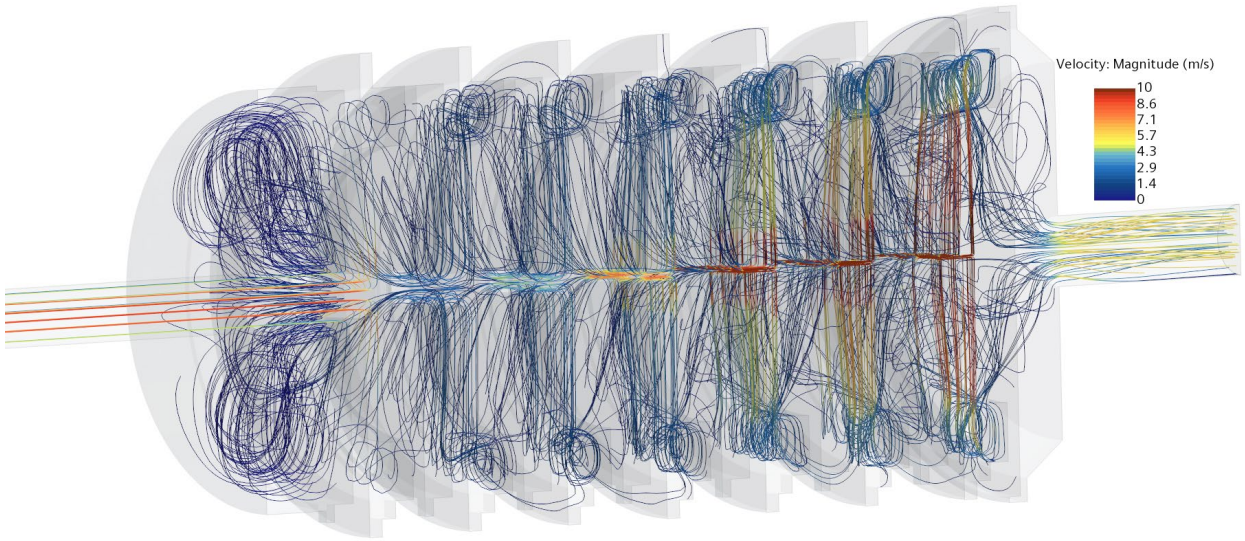

Figure I-28. Streamline plot of the flow distribution through the 7-stage cascade impactor, colored according to velocity magnitude (7 LPM).

(a)

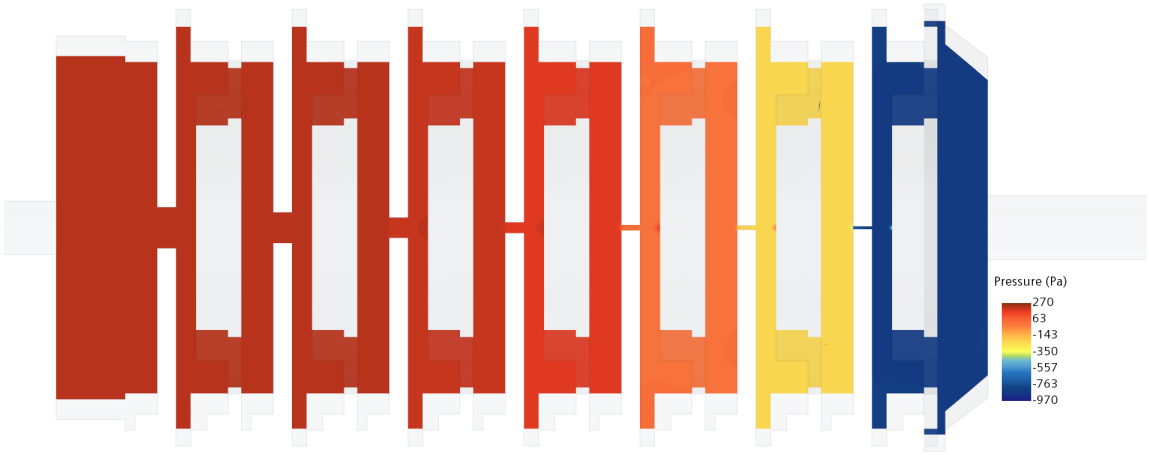

(b)

Figure I-29. Pressure contours (7 LPM) for the 7-stage cascade impactor on (a) x = 0 plane and (b) x = -8 mm plane.

A comparison of predicted and measured stage and overall pressure drops is summarized in Table I-15 for a flow rate of 7 LPM and in Table I-16 for 6 LPM. The Reynolds numbers based on D_h, only show a modest increase from stage MA to stage PD, which is similar to the results using the 4-stage impactor, albeit for an inlet flow rate of 9 LPM. For both flow rates simulated, the relative error for stages PB–PD are less than 20%, which is considered acceptable given the measurement and model uncertainties. The model uncertainties are determined by calculating the discharge coefficient, C_d, for each orifice based on mean orifice dimensions:

$$C_d = \frac{\rho U_{avg}^2}{2\Delta P}, \tag{I-9}$$

where ρ is air density (1.18415 kg/m3) and ΔP is the stage pressure drop. Assuming the discharge coefficients are the same for small deviations in orifice dimensions, the range of pressure drops is then calculated, accounting for the uncertainties in orifice length and orifice width. The model uncertainty is expected to be higher if all uncertainties are taken into account. Nonetheless, the overall pressure drop comparisons for both flow rates are excellent, and the model can be considered validated.

Table I-15. Comparison of modeled vs. experimental pressure drop values and model flow parameters for the 7-stage cascade impactor for 7 LPM.

	Simulation				Measured	
Impaction stage	U_{avg}, m/s	Re_W	Re_{Dh}	ΔP, Pa	ΔP, Pa	Absolute relative error %
Stage MA	1.69	418.2	693.5	0	0	-
Stage MB	2.20	404.1	696.0	7	0	-
Stage MC	3.24	398.1	714.5	12	30 ± 30	-
Stage PA	5.58	363.7	714.0	34 ± 1	62 ± 30	45
Stage PB	11.13	362.4	729.0	150 ± 9	128 ± 30	17
Stage PC	14.62	370.6	726.9	258 ± 20	220 ± 30	17
Stage PD	21.79	368.6	727.8	603 ± 68	675 ± 30	11
Overall	-	-	-	1116	1156	3.5

Table I-16. Comparison of model vs. experimental pressure drop values and model flow parameters for the 7-stage cascade impactor for 6 LPM.

	Simulation				Measured	
Impaction stage	U_{avg}, m/s	Re_W	Re_{Dh}	ΔP, Pa	ΔP, Pa	Absolute relative error %
Stage MA	1.43	352.9	585.2	0	0	-
Stage MB	1.90	349.6	602.2	5	0	-
Stage MC	2.82	345.7	620.5	9	18 ± 30	-
Stage PA	4.86	317.2	622.6	26 ± 1	25 ± 30	5
Stage PB	9.73	316.7	637.2	117 ± 7	99 ± 30	18
Stage PC	12.76	323.5	634.5	201 ± 15	178 ± 30	13
Stage PD	18.93	320.2	632.1	470 ± 50	481 ± 30	2
Overall	-	-	-	869	867	0.2

I-5.2 Particle Deposition Simulations

The Lagrangian modeling approach was used to investigate particle deposition on the collection plates.. The purpose of this study was to broadly capture a distribution of aerosol-sized particles and determine the mean cut point for each stage in the cascade. In the current study, solid UO_2 particles with a density of 10.97 g/cc are used. Note that all particle diameters cited within the CFD simulations are physical diameters, not to be confused with the AED specified in the cascade cut points. In the Lagrangian framework, particles are treated as parcels of mass, and applicable conservation laws are used. Lagrangian models are recommended for particle-laden flows in which the volume fraction of particles is low (less than 10%) compared with the finite-volume cell. In the Lagrangian approach in STAR-CCM+ [I-20], the equation of conservation of (linear) momentum for a material particle of mass m_p is given by

$$\mathrm{m}_p \frac{dv_p}{dt} = \mathbf{F}_s + \mathbf{F}_b, \tag{I-10}$$

where v_p denotes the instantaneous particle velocity, F_s is the result of the surface forces, and F_b is the result of the body forces. In the Lagrangian framework, the state is evolved on a particle-by-particle basis, whereas the Eulerian fields are frozen. The particle position and particle velocity are obtained by numerically integrating the position/displacement equation with time:

$$\mathrm{m}_p \frac{dr_p}{dt} = v_p, \tag{I-11}$$

where $r_p(t)$ is the instantaneous position vector at time, t. In the statistical Lagrangian approach, parcels of particles are tracked. For large particle loadings, the parcel approach can be used to save computational cost, so it is the method of choice here. A single integration of the state is applied to all particles in the parcel, and the interaction term with the Eulerian phase is calculated by multiplying by the number of particles in the parcel. For statistically converged results, it is recommended to have sufficient number of computational parcels. The surface forces can be broken down as follows:

$$\mathbf{F}_s = \mathbf{F}_d + \mathbf{F}_p + \mathbf{F}_{vm}, \tag{I-12}$$

where F_d is the drag force, F_p is the pressure gradient force, and F_{vm} is the virtual mass force. The result of the surface forces is the momentum that is transferred from the continuous phase to the particle. The body force term can be similarly decomposed as follows:

$$\mathbf{F}_b = \mathbf{F}_g + \mathbf{F}_u + \mathbf{F}_{MRF} + \mathbf{F}_{Co}, \tag{I-13}$$

where F_g is the gravity force, F_u is the user-defined body force term, F_{MRF} is applicable for moving reference frames, and F_{Co} is the Coulomb force. In the current study, F_g is the only applicable body force. There are various submodels for particle interaction forces, and these are described in detail in the Star-CCM$^+$ user manual [I-20]. In the current study, the following surface force models were selected: the virtual mass force, the pressure gradient force, the Schiller-Naumann drag force model, and the Sommerfeld shear lift force model [I-20].

To complete the Lagrangian model setup, particle injectors and particle-wall interactions must be defined. For the current study, the part injector is used with the injector properties described in Table I-17. The part injector uses the injection faces from the meshed part; that is, the inlet face. The number of injection points in the inlet face is controlled by the point inclusion probability. The total number of injection faces for the current setup was approximately 300. The number of particles per parcel (parcel streams) was

taken to be 100. The particles were injected with the same velocity as the fluid—zero slip velocity—which is a reasonable assumption that the particle movements are only driven by the pump flow. The particle flow rate was controlled by the number of injection points and parcel streams (300 × 100 per timestep). Therefore, while the specified particle flow rate was arbitrary, the total number of injections was set to inject approximately 0.5 million particles (~ 5e3 parcels) in the computational domain. The time curing which the injections occurred was controlled. The total number of injected particles in the system was selected arbitrarily, with consideration for the computational time required to ensure that the majority of the particles were collected in the collectors. A few particles escaped from the computational domain.

Table I-17. Part injector parameters

Parameters	Values
Physical particle diameter distribution	Log-normal distribution with a range of [0.1, 10] μm and a mean of 3 μm (10 μm AED)
Point inclusion probability	0.1
Parcel streams	100
Velocity	Same as fluid velocity

Four options are available in STAR-CCM+ to model particle-wall interactions: rebound, sticky, escape, and composite. In the rebound mode, particles rebound off the wall's surface and are solved using user-specified normal and tangential restitution coefficients. The sticky surface BC is the exact opposite, with particles sufficiently close to the wall sticking to the surface. The escape mode, which is not applicable for the current study, allows for the particles to escape from the boundary. The composite mode allows for a user-defined probability of the rebound, sticky, and escape modes. In the current study, all collector surfaces were defined as sticky surfaces, whereas the other wall surfaces were defined as rebound surfaces. A parameter is available in STAR-CCM+ which defines the degree to which particles stick. For this study, the particles are considered to stick if the coefficient is >= 0.8, with 1.0 defined as being completely stuck onto the surface. The locations of the part injector and the sticky boundary surfaces are highlighted in Figure I-30.

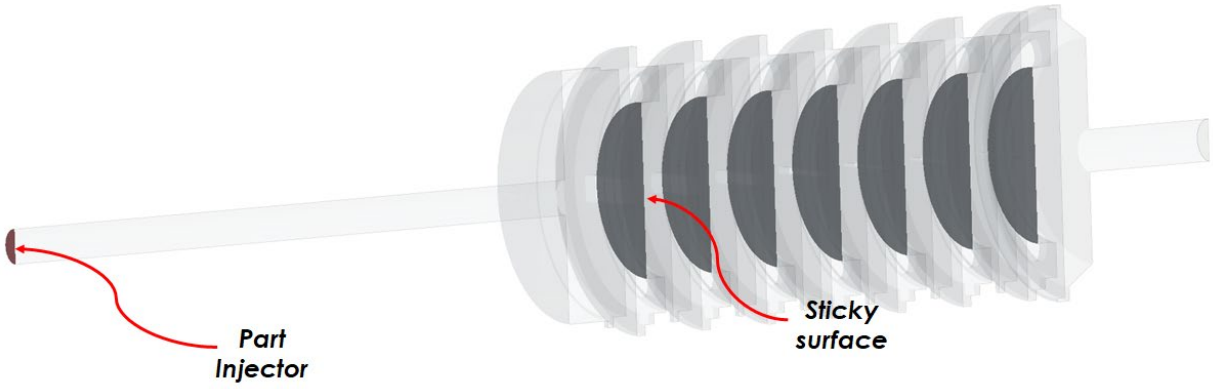

Figure I-30. Isometric view of the 7-stage cascade impactor with the (inlet) injection surface and collector surfaces highlighted.

The solution was obtained in two steps: first, the steady-state distribution for the 7-stage impactor for a flow rate of 7 LPM was obtained, and then a transient fluid solve was performed using the steady-state

distribution as the initial condition. Once the statistically converged results were obtained, the fluid solver was frozen, and the Lagrangian solver was turned on to solve for particle deposition. The transient fluid solve was conducted with a Courant number of 5. Although this might dampen physical fluctuations, a lower Courant number would be computationally expensive as a result of the much smaller time step required. For the current study, the timestep size is chosen to be 1e-4 s using a second-order implicit scheme. This approach was chosen to ensure a 1:1 timestep with the Lagrangian solver if a two-way coupling approach were required. A larger particle solver timestep resulted in poor convergence. For the Lagrangian particle solver, a second-order implicit unsteady tracking method was used with the maximum substeps capped at 1e+4 s. This ensured that the small number of parcels that had difficulty converging the particle solve were not tracked for a long time.

In the current study, all parcels converged for every time step. The particle solution was run for a physical timestep of 2 s. Although this might be insufficient to replicate the full implementation of the test method in the hot cell (estimated maximum event plus particle settling, ~300 s), the purpose of this study was to broadly capture the distribution of particles and the mean cut point for each stage. The simulation time was ~2 days running on 64 processors. Particle injection occurred within the first 100 timesteps (Δt = 1e-4), after which the injector was shut down. The final physical particle size distribution in the domain is shown as a histogram in Figure I-31. The final particle distribution is expected to follow a log-normal distribution, as defined in the injector, with only a tiny fraction of all injected particles (~0.58%) having exited from the flow domain during the course of the simulation.

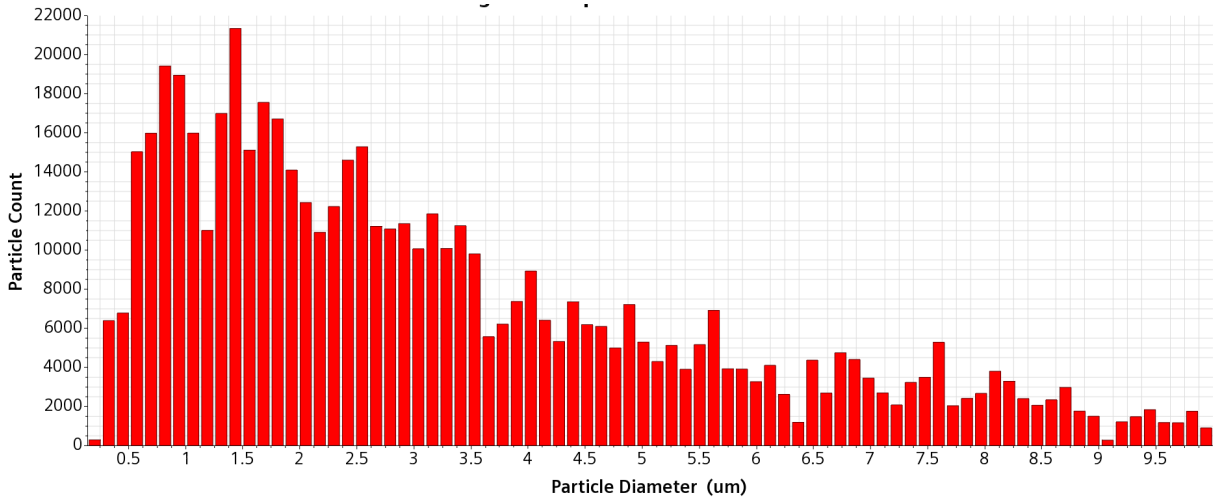

Figure I-31. Physical particle size distribution histogram in the flow domain using the log normal distribution for the injector with size range Ɛ [0.1, 10] µm and mean of 3 µm.

A snapshot of the particle distribution at the end of the simulation is shown in **Figure I-32** and Figure I-33, with particles of different sizes scaled to a fixed pixel size. After 2.5 seconds, ~95% of the total particles were collected in the 7 stages, and particle distributions were analyzed. These distributions of particles within the impinging jet area created by the orifice above are very similar to the distributions observed in physical testing; however, physical testing did not observe the large number of particles distributed on the plate at other locations.

Three observations can be made regarding the particle distribution:

1. At a flow rate of 7 LPM, the flow speeds in orifices PB-PD were high enough to force particles to collect in and around the stagnation zone

2. Stages MB and MC did not trap a lot of particles and further investigation is needed to fully evaluate their performance
3. Stage MA collected a lot of particles. This is primarily driven by the core peaked flow. Because the core peaked flow forced a high velocity jet near the center, this stage trapped particles much smaller than its designed (mean) cut point, unlike stage PD. This can be observed in the stage histogram distributions shown in Figure I-35

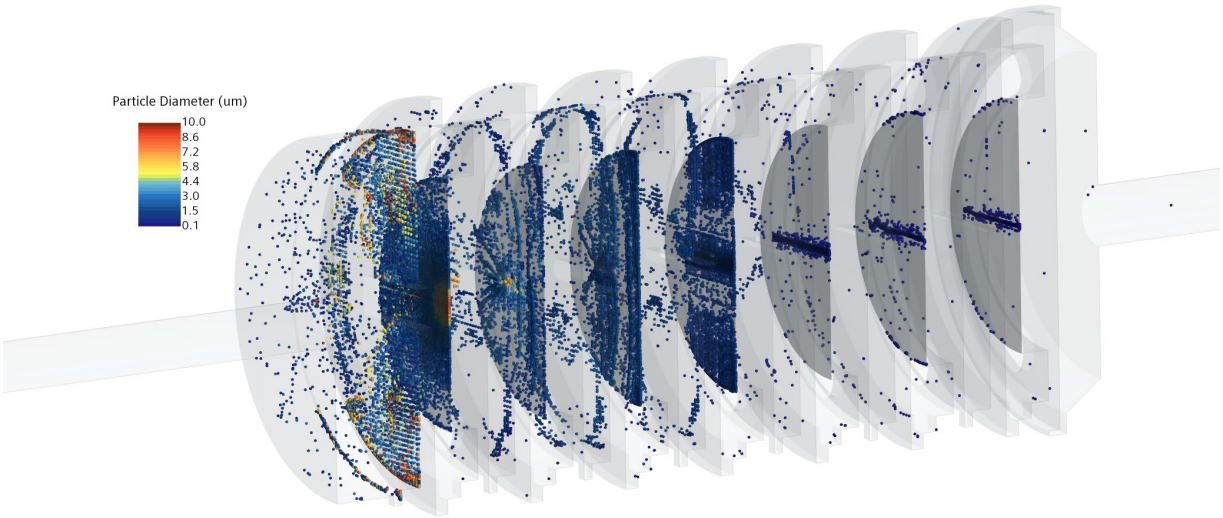

Figure I-32. Isometric view of the 7-stage cascade impactor showing the particle distribution colored according to physical particle diameter ~2.5 s after injection (7 LPM).

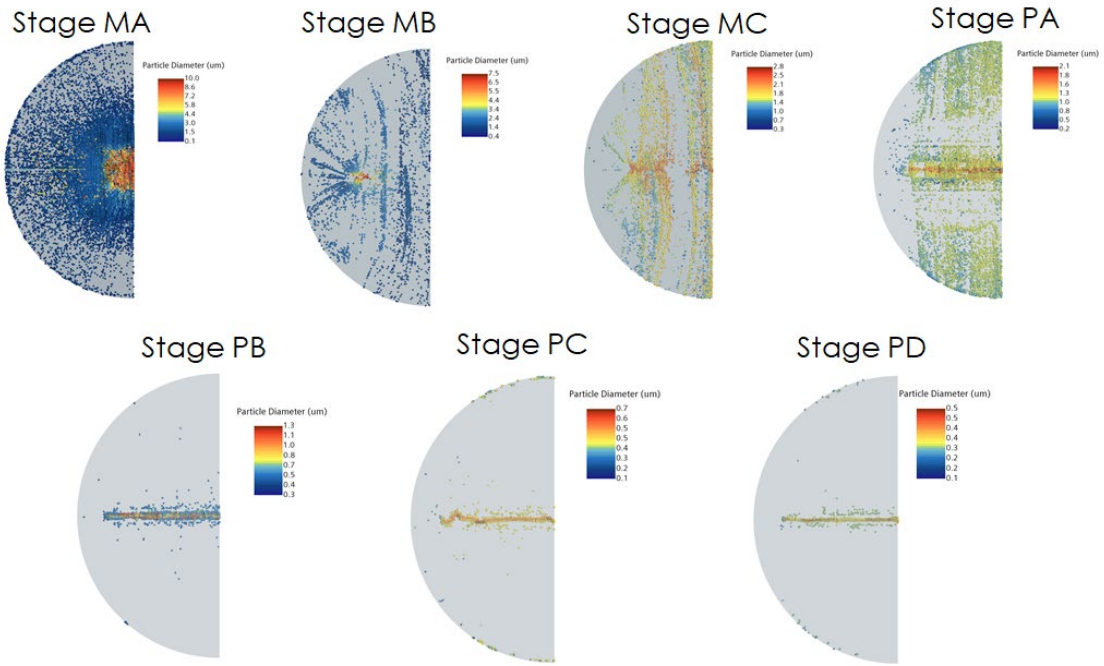

Figure I-33. Particles collected on the 7 stages at ~ 2.5 s after injection of 5.4e5 particles (7 LPM).

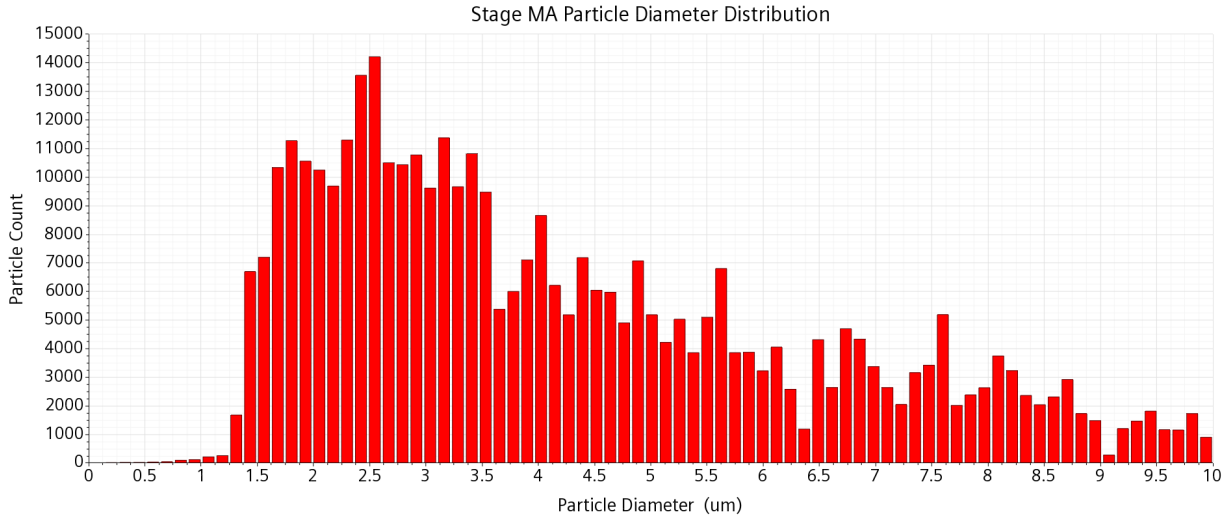

(a)

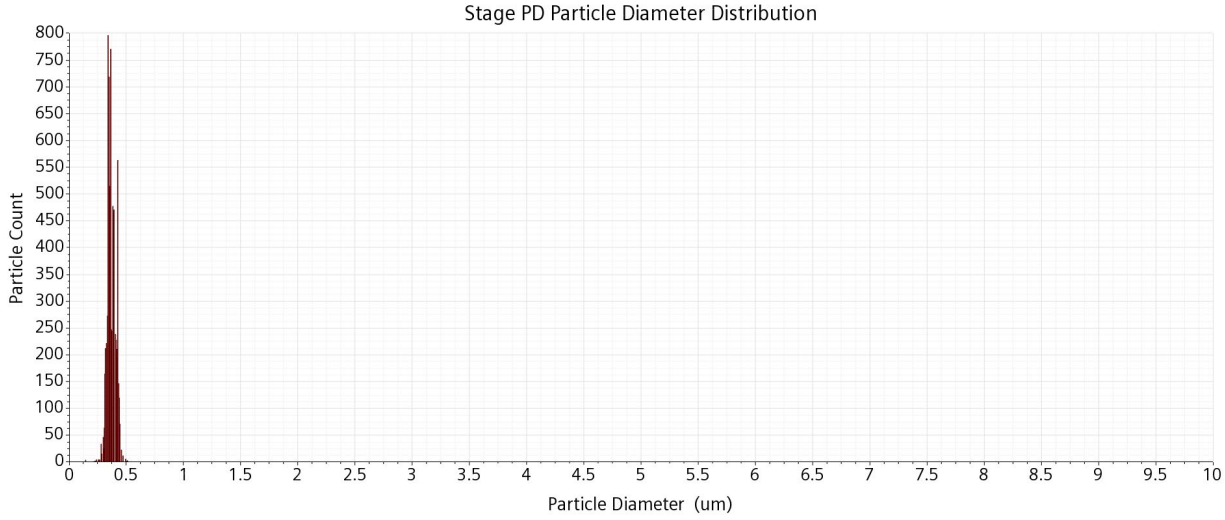

(b)

Figure I-34. (a) Physical particle size distribution histogram of particles collected (7 LPM) in (a) stage MA and (b) stage PD.

The percentages of particles collected across the 7 stages for various ranges of physical particle diameters are shown in Table I-18. Whereas stages PA–PD show sharp cut points trapping particles between 0.1–1.5 µm, stages MB–MC collect a relatively lower number of particles within the expected range, and stage MA shows a wider spread of particle sizes for reasons discussed above. The particle collection statistics are shown in

Table I-19, thus quantifying the stage cutoff diameters. The standard deviation is highest for stage MA because of a wider spread of particle sizes.

Table I-18. Percentages of particles collected across various size groups for the 7 stages (7 LPM).

		Percentages						
Size distribution (μm)								
Physical diameter, ρ=10.96 g/cc	AED	MA	MB	MC	PA	PB	PC	PD
0.1–0.25	0.33-0.83	11.8	0	0	0	0	35.3	52.9
0.25–0.5	0.83-1.66	0.2	0	0	0.1	0.3	27.2	72
0.5–0.75	1.66-2.48	0.2	0.1	0.1	0.5	69.2	29.9	0
0.75–1.0	2.48-3.31	0.6	0.3	0.1	4.9	94.1	0	0
1.0–1.5	3.31-4.97	15.2	0.9	3.2	68.4	12.3	0	0
1.5–2.0	4.97-6.62	67.3	2.2	10.1	20.4	0	0	0
2.0-2.5	6.62-8.28	93.6	2.2	4	0.1	0	0	0
2.5–3.0	8.28-9.93	97.9	1.7	0.4	0	0	0	0
>=3.0	>=9.93	99.7	0.3	0	0	0	0	0
Total number of particles collected	>=9.93	380,629	4,604	10,028	54,792	60,553	11,628	7,580

Table I-19. Particle collection statistics for the 7-stages (7 LPM).

Parameter	Stage MA	Stage MB	Stage MC	Stage PA	Stage PB	Stage PC	Stage PD
Physical mean (μm)	4.23	2.26	1.78	1.35	0.82	0.52	0.37
Physical median (μm)	3.65	2.03	1.79	1.34	0.82	0.52	0.36
Physical STD (μm)	2.15	0.84	0.31	0.22	0.14	0.05	0.04
AED mean (μm)	**14.01**	**7.49**	**5.90**	**4.47**	**2.72**	**1.72**	**1.23**
AED median (μm)	**12.09**	**6.72**	**5.93**	**4.44**	**2.72**	**1.72**	**1.19**
AED STD (μm)	**7.12**	**2.78**	**1.03**	**0.73**	**0.46**	**0.17**	**0.13**

Given the results of these simulations and the experimental observations, the added stages MA, MB, and MC are performing as expected but could be improved. As an alternative, a Marple cascade impactor has been procured, and testing of that design is underway, to be followed by corresponding simulations.

I-5.3 Collection Enclosure Simulations

Simulations of the enclosure used during aerosol collections are also being completed to determine if a substantial number of aerosols could escape collection through the openings between the 4PB fixture and the test specimen. The initial model is shown in Figure I-37 for 7L/min, indicate that this is unlikely as the fluid streamlines do not show any circulation patterns in the box. Particle simulations are required to confirm this observation. This simulation will be continued in FY22. One area of improvement could be to eliminate any static charge attraction by constructing the enclosure from metal and grounding it.

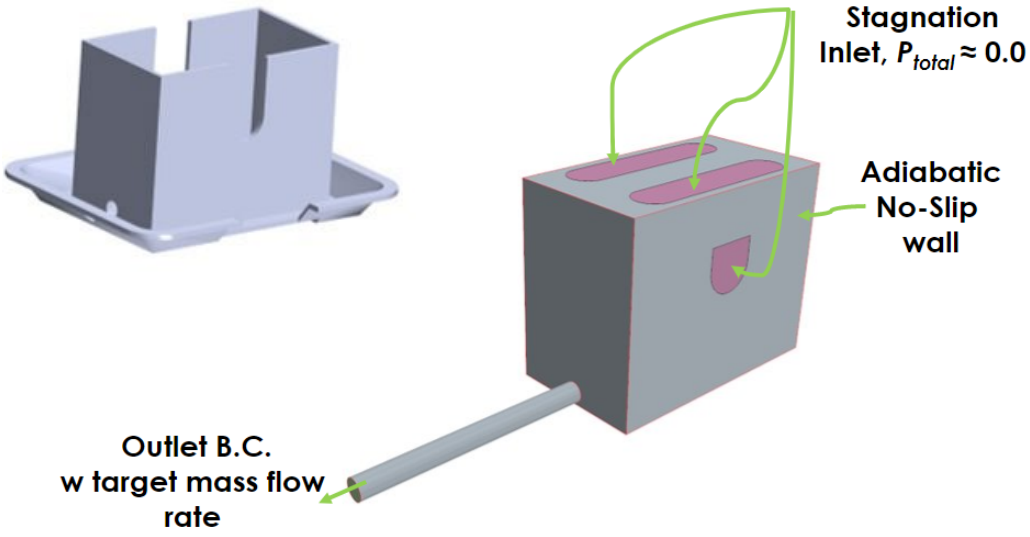

Figure I-36. CFD model of collection enclosure.

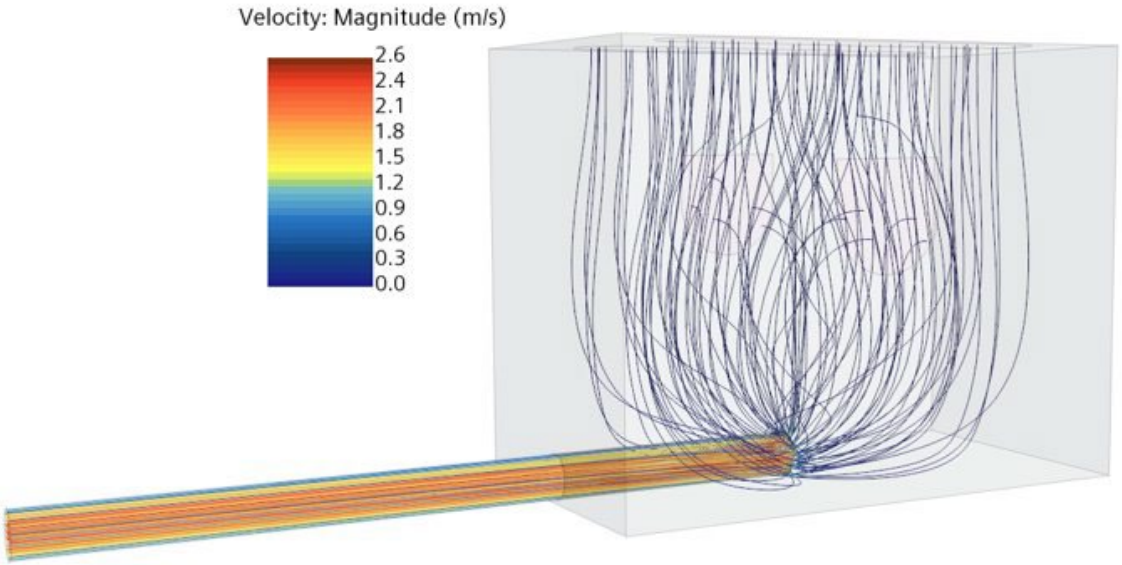

Figure I-35. Preliminary results from collection enclosure simulation indicating that there is no expected loss of particles through enclosure openings.

I-6 Aerosol Collection Test Protocol

To collect a sample, the sampling card with connected enclosure is loaded into the hot cell as a unit. The cascade is preassembled with pre-weighed carbon tabs mounted on each collection stage. The enclosure is mounted on the Instron 4PB fixture, with the rod segment placed on the lower fixture as for a normal 4PB test, and the enclosure lid placed onto the enclosure base, as shown in Figure I-38.

The sampler is energized by pushing the on/off switch just before performing the 4PB test, and the test must be completed within 15 minutes of energizing the pump to avoid lower-than-specified pump flow rates. The pump is run for 5 minutes following specimen fracture.

The upper fixture is disengaged from the enclosure, and the lid is removed. The specimens are weighed pre- and post-test to obtain a gross material loss measurement. Any large debris in the collection enclosure is collected and weighed. All inner surfaces of the enclosure are wiped, and the media are sent for chemical analysis and uranium mass measurements. Likewise, the tubing is rinsed with nitric acid, and the resulting liquid is sent for chemical analysis and uranium mass measurements. The tubing integral to

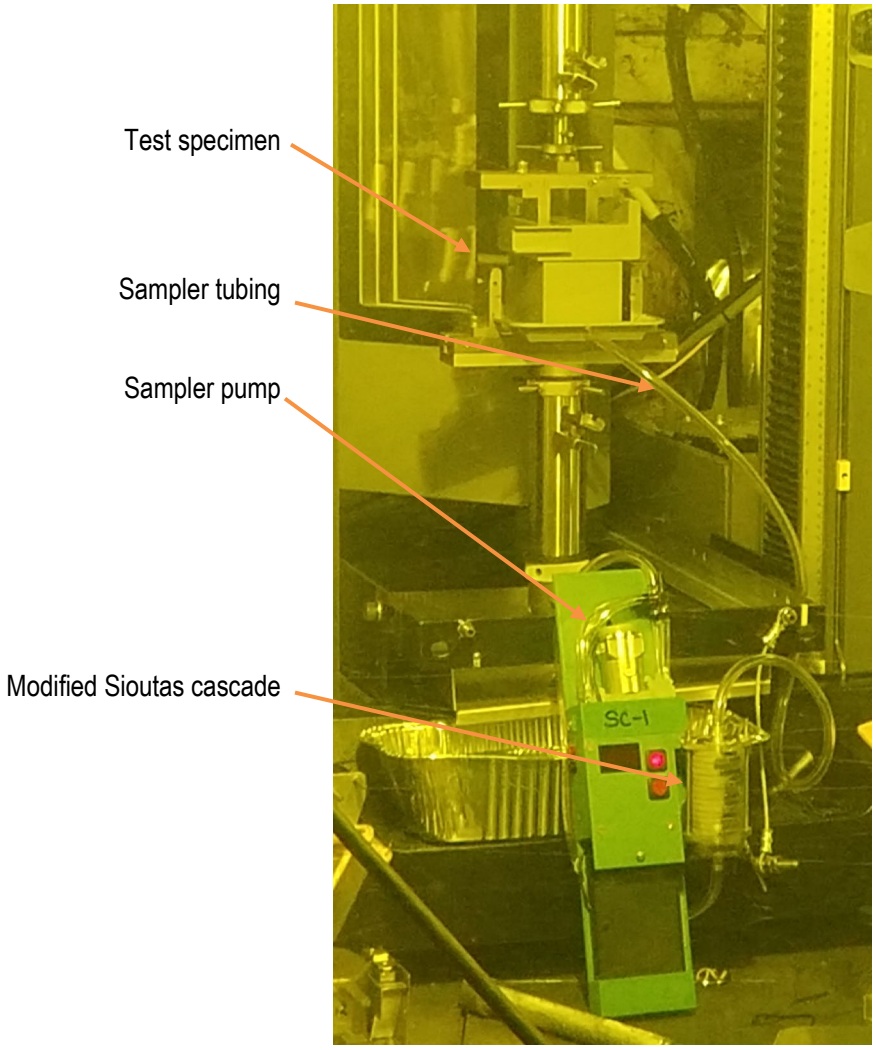

Figure I-37. In-cell 4PB aerosol sampling setup.

the miniature pump is not included, as it is not feasible to remove the tubing through in-cell manipulation. The sampling card is considered disposable, so a new one is provided for each test.

The cascade is moved to a glovebox and disassembled. Each carbon tab is extracted from the cascade and weighed. Each orifice plate is wiped down, and the material is sent for chemical processing. Smears are taken from the glovebox gloves as a potential source for contamination tracking.

Ideally, each carbon tab is then imaged using the IFEL SEM. After imaging, each carbon tab is immersed in nitric acid and transferred for chemical analysis and uranium mass measurements.

I-7 Results of SNF Test 1 Using the Modified Sioutas Cascade

In February 2021, a test of a ZIRLO-clad specimen, 3D8E14-2810-2963, was completed using the modified Sioutas cascade (7 stages) . The specimen had an estimated local burnup of 63 GWd/MTU and an average waterside cladding oxide thickness of 41 μm. The test was conducted using the protocol described in Section I-6. Figure I-38 and Figure I-39 provide post-test images of the broken rod segment.

Figure I-40 shows the beige SEM tab substrates that were isolated and mounted on SEM stubs. Unfortunately, SEM characterization was not performed on this set of samples, and the samples were loaded out for inductively coupled plasma mass spectrometry (ICP-MS). The collected SNF samples are shown as faint gray lines across the beige-colored SEM tabs, which is similar to those seen in the collections under the validation runs (Figure I-11). The SEM tabs were tapped before mounting to release any material that was not adhered. The measured mass of these specimens (material collected only) ranges from 0 to 0.006 g.

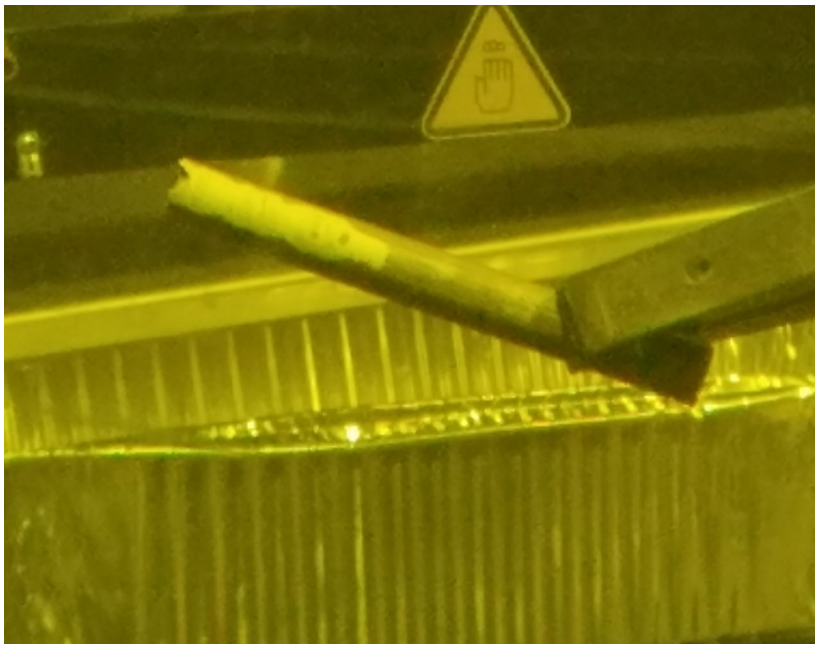

Figure I-38. Post-test fractured aerosol test specimen. Note the spalled cladding oxide in the maximum stress location.

Figure I-39. Outer surfaces of the test rod following the aerosol collection 4PB test. The fracture occurred in the body of a pellet, producing coarse debris consistent with past 4PB test results seen at ORNL.

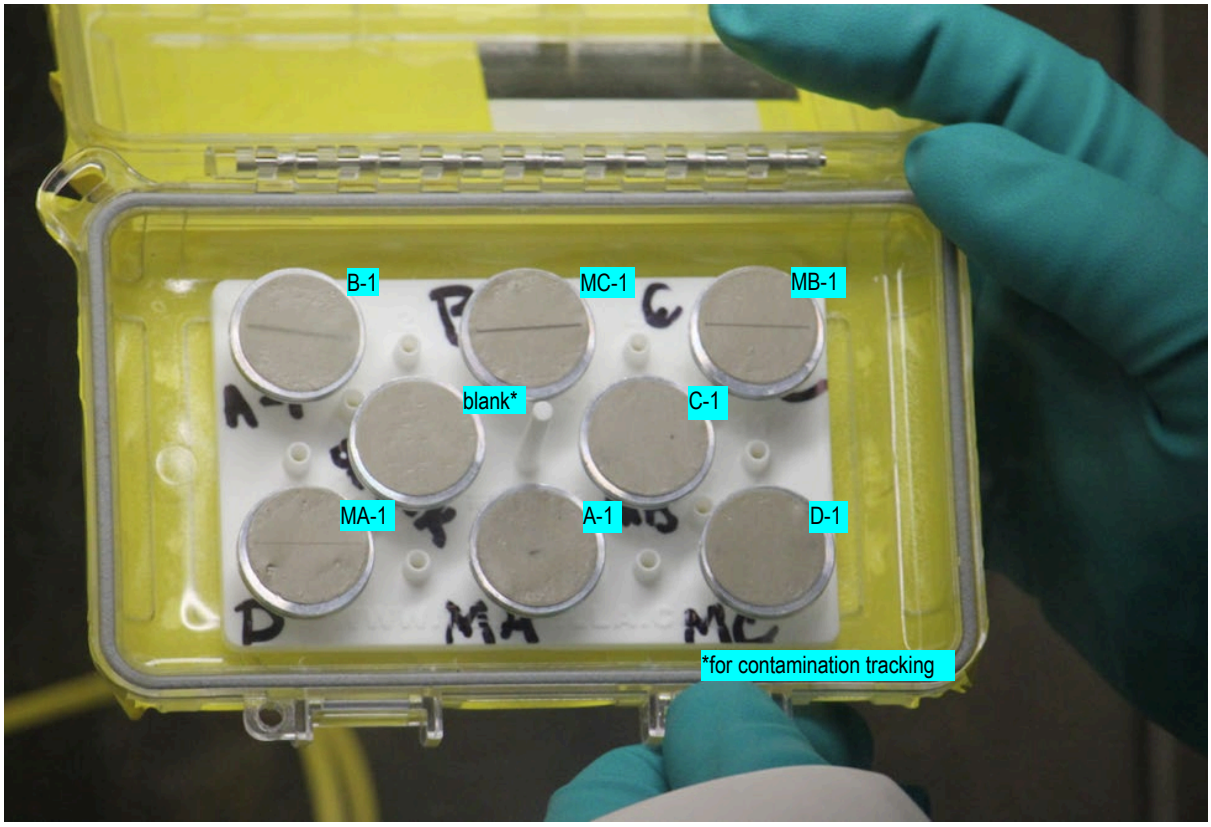

Figure I-40. SEM tabs with cascade stage markings on the background showing the aerosol collected in the experiment. Thin lines on the tabs show the collected aerosol particles from SNF.

A radiological survey (summarized in Table I-20) was conducted during the loadout after the experiment. This provided the first quantitative estimate of the collection in the cascades.

Table I-20. Dose rates from the ghost wipe smears of the impactor stages.

		Static counts from the silver tabs taken through the glove box gloves	
Collection stage	Dose rate on contact (mrad/h)	Alpha counts from plastic retaining ring (dpm/100 cm^2)	Beta/gamma counts from plastic retaining ring (dpm/100 cm^2)
MA-1	630	77,520	2,200,000
MB-1	45	38,760	2,200,000
MC-1	45	77,520	-
PA-1	5	19,379	-
PB-1	72	7,752	-
PC-1	5	9,303	-
PD-1	9	466	-

Contrary to the visible collection of particles shown in Figure I-40, the information listed in Table I-20 shows that stage MA-1 had the highest alpha dose rate. This is also consistent with the dose rates obtained from the ghost wipe smears of the impactor stages.

Unfortunately, after the test was completed, it was found that the IFEL SEM facility enclosure had gaps that needed to be closed before an aerosol-type material was brought into the room, so SEM imaging of these test specimens was not possible. The specimens were sent directly to chemical processing.

ICP-MS was used to characterize the material collected from the enclosure, tubing, and cascade stages. The analysis resulted in the detection of 29 isotopes, including isotopes of actinides U, Pu, Np, Th, Am and Cm; lanthanides La, Ce, Pr, Nd, Sm, Eu and Gd; epsilon phases Mo, Ru and Rh; and other important SNF elements such as Y, Sr, Cs, Ba and Zr. Blanks allowed counting for contaminants in the experiment, and they have been reported in the data.

Samples were received at the Radioactive Materials Analytical. Laboratory in the form of SEM silver-substrate sticky tabs and ghost wipes containing aerosol and residual fuel particles. These samples were digested using 4N-8N nitric acid solutions (Optima Grade®, Fisher) in pre-cleaned or SavillexTM PFA bottles with closures and 50 mL FalconTM tubes, respectively. The SEM tabs were also rinsed with metal-grade isopropyl alcohol to facilitate the release of adhesive and to allow access to the surface for material digestion. The SEM tab solutions were heated to 90°C with their lids on to accelerate the digestion. Once the digestion process was complete, the tabs were removed from the solution, and all solutions were analyzed by ICP-MS. The SEM tabs were monitored post-digestion for residual activity, which was detected. The tabs were then staged for ashing by muffle-furnace techniques.

The analyses of uranium, transuranic isotopes, and select fission products were performed using ICP-MS (Thermo Scientific TM iCAP TM RQ). The instrument utilizes Qtegra TM Intelligent Scientific Data Solution TM software. The mass spectrometer is positioned inside a stand-alone fume hood for radiological control and employs a standard sample introduction system using an autosampler and single-pass Peltier-cooled cyclonic spray chamber. Analyte response was made against linear regression external calibration standards from High Purity Standards (Charleston, SC) or Inorganic Ventures (Christiansburg, VA). Plutonium standard curves were made using CRM137 (New Brunswick Laboratory). Isotopes for analysis were chosen based on isobaric interferences from both natural and fission product abundances.

Neodymium and plutonium isotopic analysis for atom% determinations were made using HP-IC-ICPMS (high-pressure ion chromatography ICP-MS) using Thermo Scientific TM iCAP TM Q coupled with DionexTM CS5000 gradient pump and off-the-shelf chromatographic separation columns. A mixed-gradient elution profile using diglycolic acid (100 mM), oxalic acid (150 mM), and deionized water to make up the gradient concentrations was used to separate isobaric interferences from the target Nd and Pu isotopes.

Table I-21 provides a summary of the separations process used, and Figure I-42 provides a diagram of the process.

Table I-21. Eluent profile for separation of Nd, Pu from isobaric interferences.

Segment type	Segment duration (s)	Segment end time (s)	Deionized water (%)	2 M hydrochloric acid (%)	0.1 M diglycolic acid (%)	0.15 M oxalic acid (%)
Start	0	0	100	0	0	0
Ramp	300	300	40	0	0	60
Hold	240	540	40	0	0	60
Ramp	0	540	20	0	0	80
Ramp	540	1,080	51	0	26	23
Ramp	120	1,200	0	0	100	0
Hold	300	1,500	0	0	100	0
Ramp	0	1,500	0	100	0	0
Hold	120	1,620	0	100	0	0
Ramp	120	1,740	100	0	0	0
Hold	60	1,800	100	0	0	0

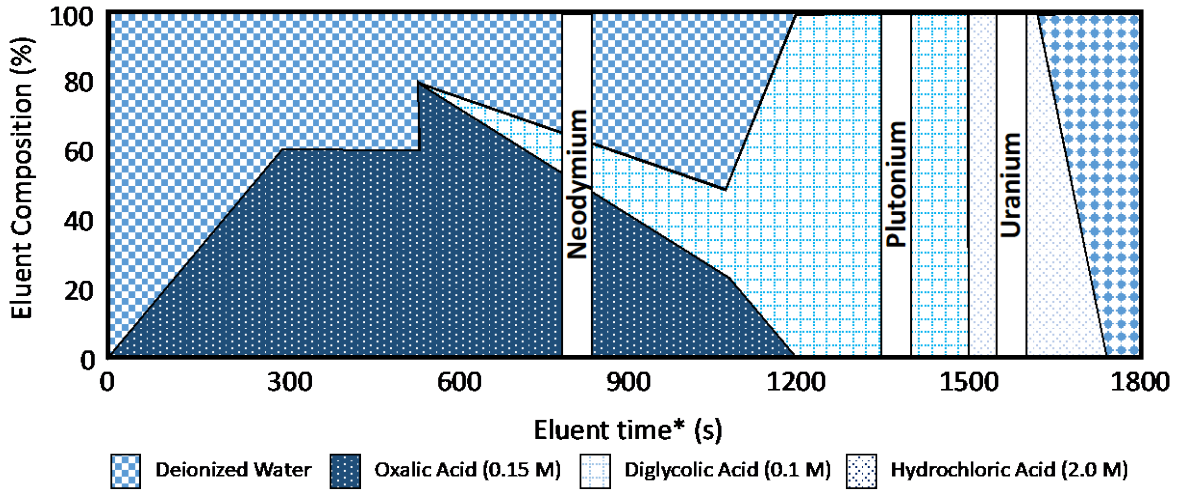

Figure I-41. Graphical representation of chromatographic separation real-time analysis. Times are approximate, because real-time shifts can result from chemical matrices.

Table I-22 summarizes the total mass recorded for the dust collected from each surface in the flow path. The coarse SNF debris collected after the test was 0.5 g, which is the same as the recorded loss from the specimen post-test, within the capabilities of the scale used at ±0.1 g. The total mass of SNF collected from the experiment is 4,615.85 µg. Within the errors of the mass measurement technique, it was observed that the collection box yielded the maximum mass of dust-sized particulate, which was 15 times more than that collected in the cascade impactor. The lid also held a significant amount of SNF dust particulate, and the lowest mass of dust particulate was obtained from the tubing that connected the collection box and the cascade.

Table I-22. Collected mass total using ICP-MS.

Stage	Total, µg	Uncertainty, µg.	Relative error (%)
MA-1	84.53	7.92	9.4
MB-1	93.43	8.40	9.0
MC-1	28.02	2.59	9.2
A-1	26.57	2.36	8.9
B-1	24.31	2.22	9.1
C-1	9.10	0.80	8.8
D-1	2.12	0.17	8.3
Lid	85.54	6.60	7.7
Base	3988.74	332.58	8.3
Tubing	47.19	3.31	7.0
MA-1 orifice plate	150.9	14.4	9.5
MB-1 orifice plate	46.2	4.4	9.5
MC-1 orifice plate	17.8	1.7	9.6
A-1 orifice plate	4.8	0.4	8.3
B-1 orifice plate	3.4	0.3	8.8
C-1 orifice plate	1.8	0.1	5.6
D-1 orifice plate	1.4	0.1	7.1
Total mass collected as dust-type particulate	4615.85	388.35	8.4

Figure I-42 gives the total mass of particles collected in each stage of the impactor. MA-1 and MB-1 collected the largest mass of particles, ranging between 80 and 100 µg. MC-1, MA-1 and MB-1 collected similar amounts, ranging between 20–35 µg. PC-1 and PD-1 collected the least amount of aerosols at under 20 µg. The impactor was designed to collect aerosols based on particle sizes, and in the absence of an SEM characterization, the trends in the total mass of particles collected can give an estimate of the total volume of SNF particles collected in each stage.

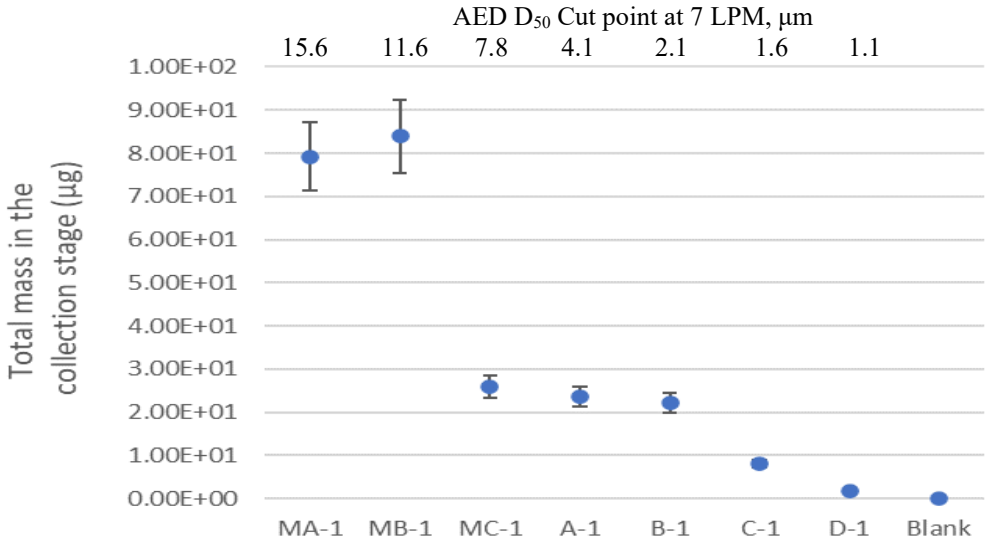

Figure I-42. Total mass collected on the filters.

Previous experiments involving aerosol production and characterization using SIMFUEL have shown preferential particle size formations based on composition and multiphase particle formations [I-21]. Although characterizing these features would require an SEM/EDX analysis, the trends in individual isotopic data have been used to discuss the implications of such characteristics in real SNF. These hypotheses will be validated in future experiments involving a thorough SEM characterization of the collected particles. Figure I-43 provides is the distribution of ^{238}U in each of the stages, and it trends well with the total mass collected (Figure I-42). MA-1 and MB-1 have the highest collection compared to the other stages. However, the graph is not consistent with the visual information presented in Figure I-40; this discrepancy may be a result of a limited number of large SNF particles that contribute to the total mass compared to the thicker distribution of smaller particles observed in the subsequent stages.

Figure I-44, Figure I-45, and Figure I-46 show the distribution of lanthanides ^{140}Ce, ^{139}La, and ^{146}Nd. Lanthanides are generally observed to form solid solutions with the actinide oxides, as can be observed from the distribution of ^{146}Nd, which follows that of ^{238}U. However, ^{139}La and ^{140}Ce seem to have no similarity in distribution or resemblance to that of uranium, which suggests that their region of origin differs from than that of Nd.

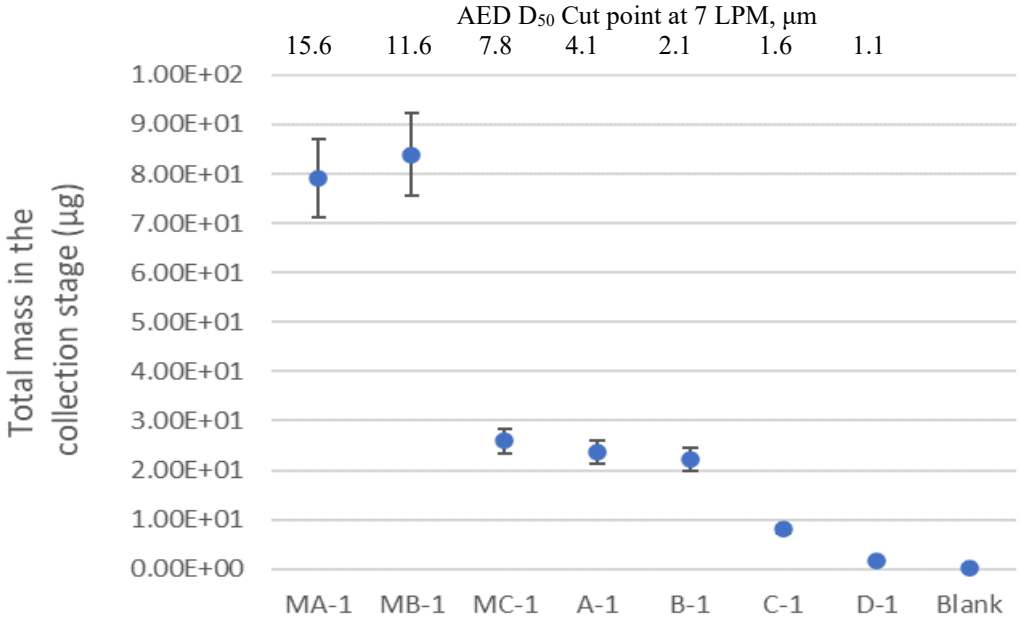

Figure I-43. ^{238}U distribution in the cascade stages.

Figure I-47 shows the distribution of ^{137}Cs in the cascade. The release trend resembles that of ^{238}U, with MA-1 and MB-1 having the highest release, followed by MC-1, A-1, B-1, C-1, and D-1. The graph is consistent with the high beta/gamma values recorded in Table I-20. Cesium is highly volatile and is found mainly in grain boundaries and gaps of the fuel pellet. Figure I-48 compares the distribution trends of actinides in each of the impactor stages. It is observed that they follow the same distribution and hence can be understood as agglomerations or solid solutions of actinide oxides being released from the fracture. SEM characterization is required to ascertain the exact release pattern. Figure I-49 shows the distribution trends in epsilon particles collected in each stage. The distribution of ^{91}Zr is also provided as an indication of noble metal content from the cladding [I-22]. A similar trend can be seen in the lower AED stages, suggesting some smaller particles have attached themselves to larger particles.

During chemical processing, the SEM tabs swelled and captured some particulate in the matrix. To fully characterize the mass of isotopes deposited, it may be necessary to ash the SEM tabs; the masses reported here many be inaccurate. Further analysis is in progress to digest these substrates. Future experiments will also involve SEM / energy-dispersive x-ray (EDX) characterization to gain a better understanding of particle size distribution and the nature of particles collected.

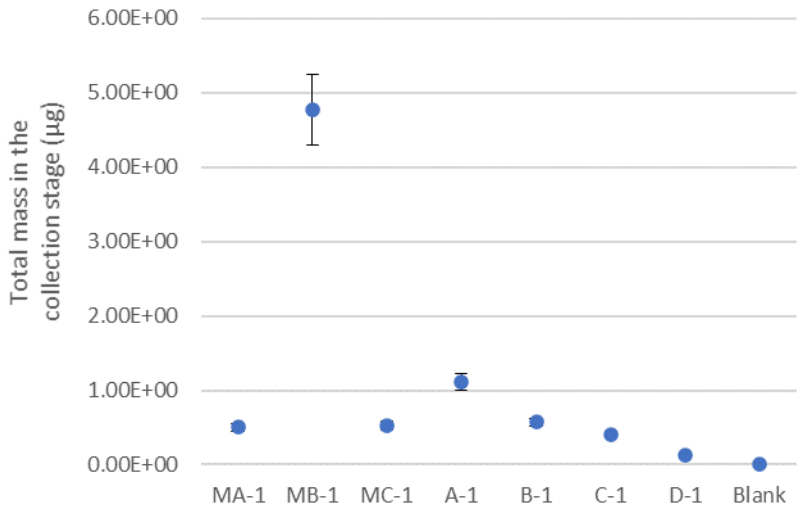

Figure I-44. ^{140}Ce distribution in the cascade stages.

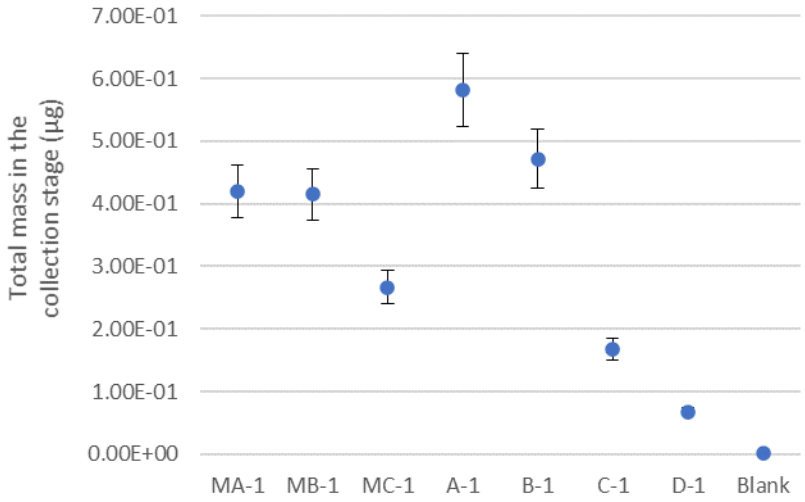

Figure I-45. ^{139}La distribution in the cascade stages.

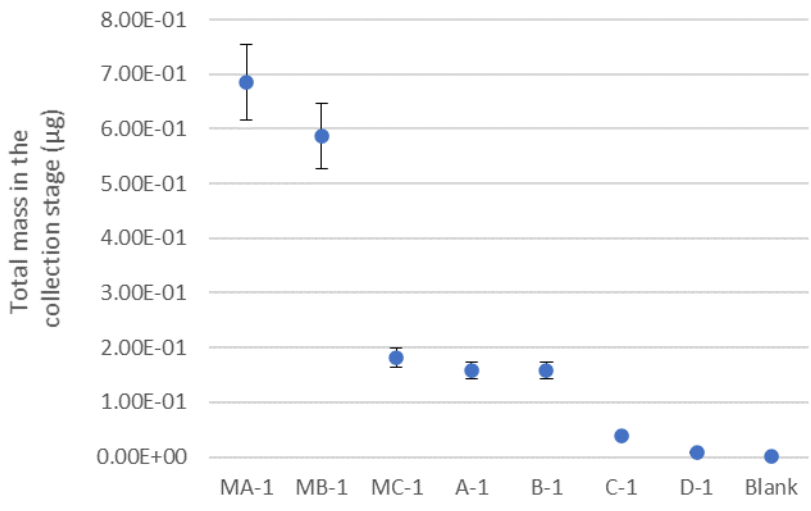

Figure I-46. ^{146}Nd particle distribution in the cascade stages.

AED D_{50} Cut point at
7 LPM, µm
MA-1, 15.6
MB-1, 11.6
MC-1, 7.8
A-1, 4.1
B-1, 2.1
C-1, 1.6
D-1, 1.1

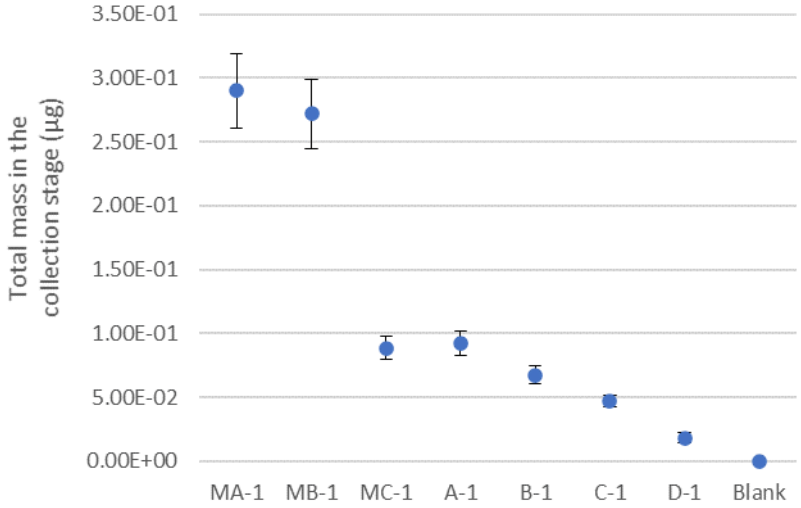

Figure I-47. ^{137}Cs particle distribution in the cascade stages.

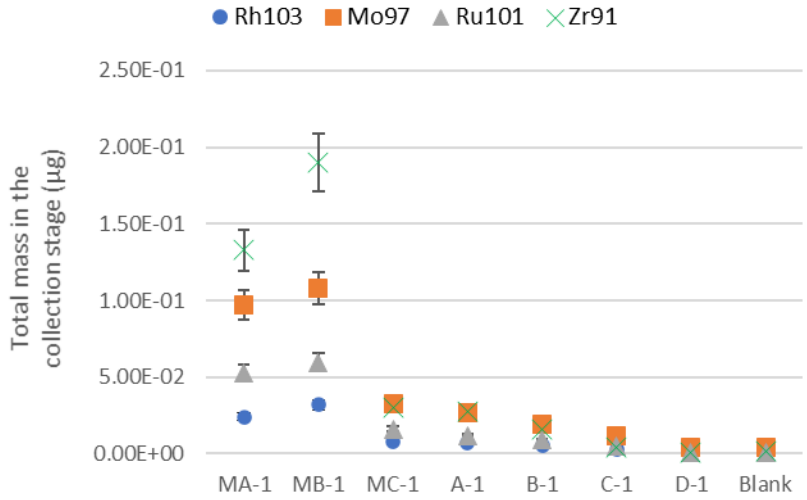

Figure I-49. Epsilon particle distribution in the cascade stages, presented along with ^{91}Zr for comparison.

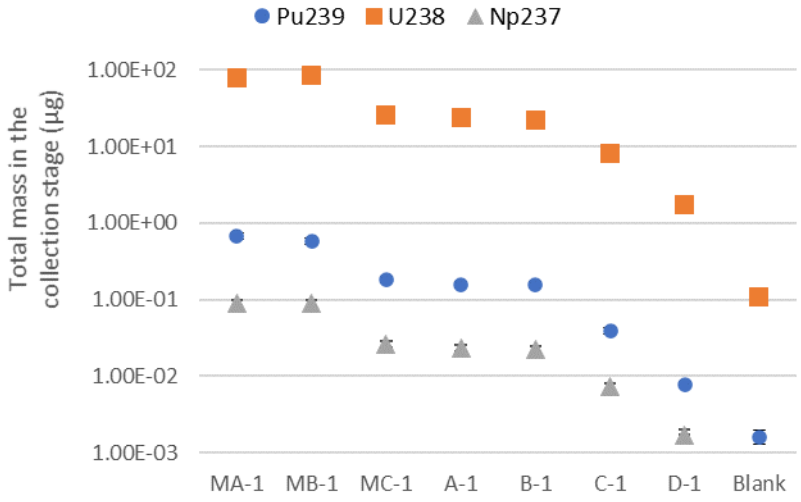

Figure I-48. Actinide particle distribution in the cascade stages.

AED D_{50} Cut point at
7 LPM, µm
MA-1, 15.6
MB-1, 11.6
MC-1, 7.8
A-1, 4.1
B-1, 2.1
C-1, 1.6
D-1, 1.1

I-8 Future Work

ORNL has obtained some Marple cascades (Figure I-50) and will test them for potential use in future experiments. The Marple cascade has higher stage cut points than those available using the Sioutas cascade impactor. The validation of this impactor using ISO dust powder is underway.

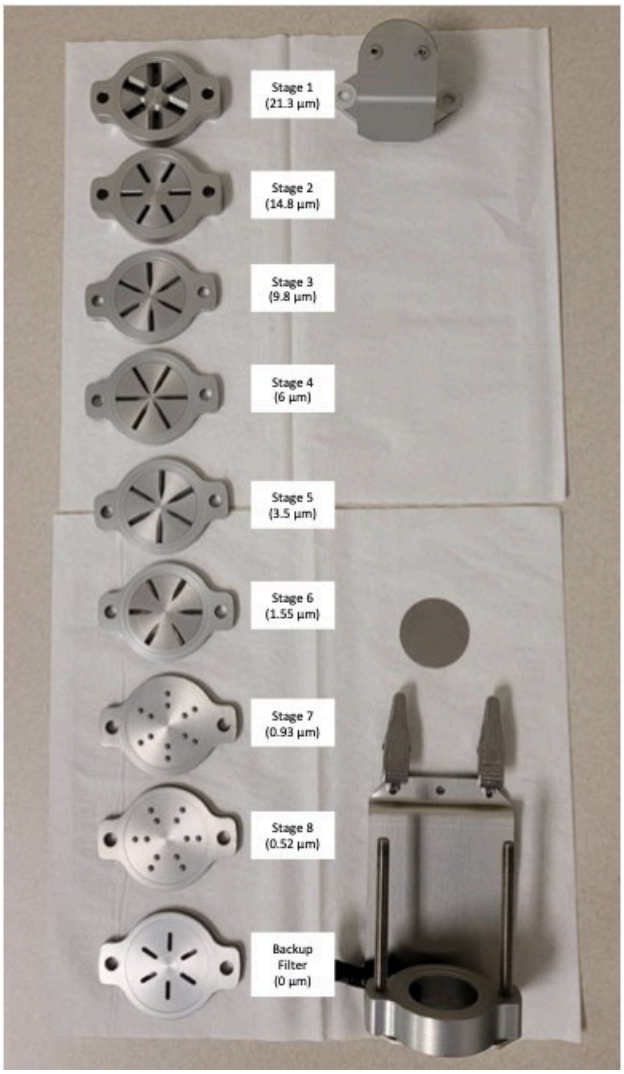

Figure I-50. Disassembled Marple impactor with respective cut-off values for each stage.

Analysis of the material collected during test 1 will continue. The SEM suite in IFEL has been backfit to allow for entry of aerosols, and imaging will be completed for future specimens collected. Table I-23 provides a summary of the planned tests for aerosol collection.

To collect the aerosols released during fatigue fractures, a collection enclosure is being designed for the CIRFT machine.

Table I-23. List of specimens tested in 4PB where aerosols are planned to be collected.

Specimen ID	Cladding alloy	Test temp. (°C)	Specimen heat treatment before test	In-reactor operating zone	Specimen average burnup (GWd/MTU)	Specimen average oxide thickness (μ)
30AD05-1003-1156	M5	RT	None	zone1	60	3
30AE14-1800-1953	M5	RT	FHT	zone1	60	9
3D8E14-2810-2963 [a]	ZIRLO	RT	None	zone1	63	41
3F9N05-2882-3035	ZIRLO	RT	FHT	zone1	58	46
3A1F05-2402-2555	LT Zirc-4	RT	None	zone1	55	117
F35P17-2402-2555	Zirc-4	RT	FHT	zone1	52	117

FHT = full-length fuel rod heat treatment

[a]Test complete; analysis ongoing

References

[I-1] *High Burnup Dry Storage Cask Research and Development Project: Final Test Plan*, contract no. DG-NG-0000593, Electric Power Research Institute, Palo Alto, California (2014).

[I-2] S. Saltzstein et al., *Visualization of the High Burnup Spent Fuel Rod Phase 1 Test Plan*, SAND2018-8042-O (2018).

[I-3] R. A. Montgomery et al., *Post-Irradiation Examination Plan for High Burnup Demonstration Project Sister Rods*, SFWD-SFWST-2017-000090 ORNL/SR-2016/708, Oak Ridge National Laboratory, Oak Ridge, Tennessee (2016).

[I-4] NUREG-2125, Spent Fuel Transportation Risk Assessment, Final Report, 2014, pp. E21-22.

[I-5] C. Sioutas, *Development of New Generation Personal Monitors for Fine Particulate Matter (PM) and Its Metal Content*, NUATRC Research Report 2 (2004).

[I-6] Marple, V. A. & Willeke, K. Impactor design. Atmos. Environ. 10, 891–896 (1976).

[I-7] SIEMENS, *STAR-CCM+ Simcenter Documentation 2021.1* (2021).

[I-8] Hinds, W. C. Aerosol Technology: Properties, Behavior, and Measurement of Airborne Particles. Wiley (1982).

[I-9] United States Patent US006786105B1, Personal Particle Monitor (2002).

[I-10] M. E. Moore and Y. Tao, *Aerosol Physics Considerations for Using Cerium Oxide CeO_2 as a Surrogate for Plutonium Oxide PuO_2 in Airborne Release Fraction Measurements for Storage Container Investigations*. Los Alamos National Laboratory (2017).

[I-11] Hinds, W. *Aerosol Technology Properties , Behavior , and Measurement of Airborne Particles Second Edition*, Wiley (2012).

[I-12] Aerosol Science and Technology - Parker C. Reist, McGraw-Hill, 1811, https://books.google.com/books/about/Aerosol_Science_and_Technology.html?id=ZEcvAQAAIAAJ.

[I-13] Mathworks MATLAB Image Processing Toolbox

[I-14] Bansal, S. & Maini, R. A Comparative Analysis of Iterative and Ostu's Thresholding Techniques. *Int. J. Comput. Appl.* 66, 975–8887 (2013).

[I-15] Singh, T. R., Roy, S., Singh, O. I., Sinam, T. & Singh, K. M. A New Local Adaptive Thresholding Technique in Binarization, *IJSCI* (2012).

[I-16] Find edges in intensity image - MATLAB edge. https://www.mathworks.com/help/images/ref/edge.html.

[I-17] Morphological reconstruction - MATLAB imreconstruct. https://www.mathworks.com/help/images/ref/imreconstruct.html?searchHighlight=imreconstruct&s_tid=srchtitle.

[I-18] Marker-Controlled Watershed Segmentation - MATLAB & Simulink Example. https://www.mathworks.com/help/images/marker-controlled-watershed-segmentation.html.

[I-19] I. Arganda-Carreras et al. "Trainable Weka Segmentation: a Machine Learning Tool for Microscopy Pixel Classification." Bioinformatics 33, 2424–2426 (2017).

[I-20] SIEMENS, STAR-CCM+ Simcenter Documentation (2021).

[I-21] F. G. Di Lemma, J. Y. Colle, G. Rasmussen, and R. J. M. Konings, "Fission Product Partitioning in Aerosol Release from Simulated Spent Nuclear Fuel." *J. Nucl. Mater.* 465, 127–134 (2015).

[I-22] R. A. Clark et al. "Distribution of Metallic Fission-Product Particles in the Cladding Liner Of Spent Nuclear Fuel." *NPJ Mater. Degrad.* 4, 4 (2020).